Seismic velocity structure of the shallow part of the Alpine fault and gravity study of the basement features in the Whataroa River flood plain, central Westland, South Island

---

Nicolas Brikke supervised by Tim Stern

Submitted as partial fulfillment of a Graduate Diploma in Science in Geophysics at the Institute of Geophysics of Victoria University of Wellington, New Zealand

Wellington, December 2007

Frontispiece

For the Ngāi Tahu, the southern Māori people, the rise of the Southern Alps ("Kā Tiritiri o te Moana" in Te Reo Māori) is described by the following legend as stated in Coates [2002]:

> When still no land existed where New Zealand is nowadays, Aoraki and his three brothers Rakiroa, Rakirua and Rārakiroa were rowing away from their home land in their waka to find new ground to settle onto. While heading back to the northern waters from the deceiving quest they got stuck and capsized on a shallow reef. The vessel settled as the four brothers leaned over the portside to balance it. They maintained this position for so long that they turned to stone and earth. The tipped over part of the waka became the mountain range known as the Southern Alps and the four brothers, whose heads and bodies stick out the side of the embarkation, impersonate its four highest peaks.

Therefore the South Island, also called "Te Wai Pounamu" (the Jade water), carries the name of "Te Waka o Aoraki" (Aoraki's Canoe). And Mount Cook's, Mount Dampier's, Mount Teichelman's and Mount Tasman's Māori names are respectively Aoraki, Rakiroa, Rakirua and Rārakiroa.

This legend makes Ngāi Tahu the first people to admit the concept of the clockwise rotation (looking north) of the uplifted rocks of the Southern Alps along the fault plane of the Alpine fault.

Acknlowledgements

I would like to express my regards to my supervisor Tim Stern. The enthusiasm, encouragement and knowledge passed on to me made a considerable positive difference in the outcome of this project. My gratitude also goes towards Euan Smith whose inspiring chats and mindful understanding were very much appreciated. Coming from a Biology background made the learning curve steep and rugged, but both of you participated strongly in smoothing it out and in transforming Geophysics into a passion.

I am grateful for the contributions of Tim Little from the School of Geography, Environment and Earth Sciences at Victoria University of Wellington (VUW) and of Mark Rattenbury from the Institute of Geological and Nuclear Sciences in Lower Hutt (GNS) for supplying a geological touch to the project and for reminding me that, behind the computer screen and the numbers, it is rocks that we are dealing with. I also acknowledge the help of Frederick Herman from the Research School of Earth Sciences at the Australian National University and that of Jim Pearce from the School of Chemical and Physical Sciences at VUW.

A warm thank you to all the PhD, Masters and graduate students at VUW who were always helpful in times when the computer was on the edge of being thrown out the window. Special thanks to Erik, Adrian, Wanda, Michelle, Dr. Henderson, Sandra, Rob Davies, Anya, Jesse, Sonja, Suzannah, Raj, Sanjay, Sonu, Ayelen y Niko Schiavi, Rachel, Dan, Frances, and Jessica.

I am ever-thankful for the trust and support that my parents and sister have shown me throughout my life. Last but certainly not least, thank you Matilda, my other half, for your infinite kindness and precious presence without which I surely would not be what I am today. I dedicate the fruit of my efforts to you.

Abstract

The deep and middle sections of the Alpine fault have extensively been studied, however, the shallow part has had relatively minor geophysical attention. This study focuses on the basement geometry and the determination of the upper-crustal velocity structure of the Alpine fault in the vicinity of the Whataroa River flood plain in Central Westland, South Island. Data from a temporary gravity survey collected in November 2006, the GNS gravity database and four of the westernmost shot gathers from the SIGHT96's transect 1 were used for this project. A ray-tracing software was used to establish the velocity structure of the shallow part of the Alpine fault. Seismic velocities decrease to 3.8 km/s immediately southeast of the mylonite strip, which is adjacent to the Alpine fault's ramp heading towards the fault's surface trace from the southeast or from depth. Velocities of 5 km/s reach 2 km depth to the southeast of the Alpine fault's ramp. Results of the gravity and seismic models coincide in the positions and the dimensions of two northwest-orientated glacial overdeepings. The strike of their alignment is offset to the northeast by 3.5 km and is sub-parallel to the mouth of the Whataroa River. We propose that these kettle holes, thought to have been carved successively during the Waimea and Otira glaciations, are the beheaded river mouth of the Whataroa river. By supposing that the furthest kettle hole was carved during the Waimea glaciation, the 3.5 km offset thus corresponds to 140 Ka of dextral slip on the Alpine fault, we could approximate the mean displacement rate over the time interval of 140 – 18 Ka of 25 mm/yr.

Contents

List of Figures

List of Tables

Chapter 1

Introduction

1.1 Motivation for this project

The central South Island of New Zealand is physiographically dominated by the Alpine fault and the associated Southern Alps. Both transcurrent (35 mm/yr) and convergent motions (10 mm/yr) are thought to be taken up or adjacent to Alpine fault. There is general agreement that the Alpine fault has an associated Low Velocity Zone (LVZ) [Davey et al. 1998, Leitner et al. 2001, Smith et al. 1995, Stern and McBride 1998], which Stern et al. [2001] modelled to be three times longer in the down-dip direction than in the across-dip one. Garrick and Hatherton [1973] brought evidence of the extent of the low seismic velocities at the surface and as complement Stern et al. [2001] ensures that the high-fluid-pressure-induced LVZ reaches depths as shallow as 8 km. However, little is known about the velocity structure between the surface and 8 km depth in the direct vicinity of the Alpine fault. This thesis presents a new image of the shallow part of the Alpine fault by building a seismic velocity structure derived from seismic refraction data. This thesis will also aim to shed some light on the basement geometry of the Whataroa River flood plain using both seismic and gravity modelling.

1.2 The West Coast geological setting

The West Coast of the South Island of New Zealand coincides with an absence of seismicity, elsewhere omnipresent in New Zealand. It is delimited on the southeast by the Alpine fault, with the parallel running Southern Alps, and on the northwest by the Tasman Sea. About 30 km north of Franz Josef township and 70 km south of Hokitika lies the Whataroa River flood plain, the study area for this project (figure 1.1). It is bound to the west, east and northeast by lateral glacial moraines [Suggate and Almond 2005]) and to the south by the Price Range, that reaches 1000 m.a.s.l. less than 1 km from the Highway 6.

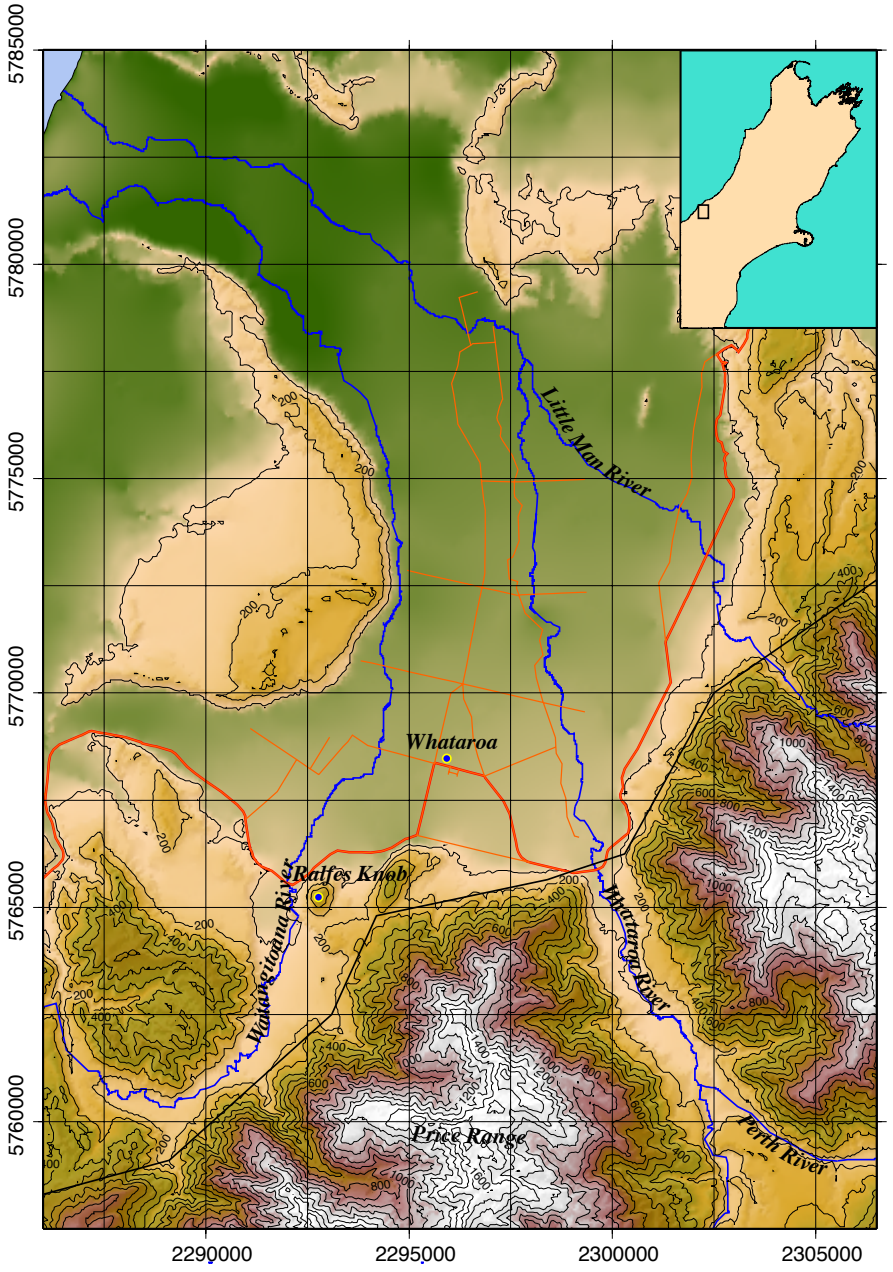

Figure 1.1: Topographical map of the study area, showing the Whataroa township, the Highway 6 (thick red line) and the farm roads (thin red line). The Waitangitoana River, Whataroa River, Perth River and Little Man River (also known as Dry Creek) are drawn and labeled. Two granitic intrusions are found to the north of the Price Range, one is called Ralfes Knob, the other is nameless. The thin black line is the assumed location of the Alpine fault's surface trace.

1.2.1 General New Zealand tectonics

New Zealand lies on the tectonic boundary between the Australian Plate on the west and the Pacific Plate on the east. The latter subducts under the Australian plate along the Hikurangi Trough terminating north of Kaikoura. There, an oblique-compression motion occurs through a set major faults in the northern South Island and along the Alpine fault. The latter extends to the south into the Puysegur Trench offshore of Fiordland, where the northern subduction pattern reverses its polarity [Davey and Smith 1983, Suggate 1963].

Plate motion

While plate motion on the Alpine fault was dominated by a strike slip motion until about 7 Ma, significant convergence started and increased since then [Walcott 1998]. The current estimates of the motion rates are as follows:

- **Parallel motion:** An average rate of 36 – 39 mm/yr (NUVEL-1A) [Beavan et al. 1999, Walcott 1998] led to 850 km of dextral slip, 460 km of which have been accommodated along the Alpine fault [Sutherland 1999].
- **Perpendicular motion:** A rate of 9 – 12 mm/yr [Beavan et al. 1999, Walcott 1998] led to 100 km of east-west shortening of the South Island [Walcott 1998] with an estimated 19 km of crustal section uplifted along the Alpine fault [Tippett and Kamp 1993].

Main Faults

Major faults such as the Fraser fault [Jongens 2006, Young 1968] and the Bald Hill Ranges Thrust fault [Rattenbury 1986] are to be found on the West Coast but not in the Whataroa flood plain. The Alpine fault, which is a prominent feature in the area is:

- continuous for more than 500 km and is aligned with the Main Divide of the Southern Alps [Sutherland 1999];
- thought to accommodate 70% of the plate motion [Norris and Cooper 1995];
- dipping at about 40° [Davey et al. 1995, Kleffmann 1999] and is expected to steepen towards the surface [Braun and Beaumont 1995];
- and thought to be composed, on the scale of a few kilometers, by north and east-orientated segments dominated by oblique thrusting and strike-slip motions, respectively [Norris and Cooper 1995].

Crustal thickening

The crust, which is 25 – 30 km thick to the east and west of the South Island, reaches thicknesses of 37 – 44 km 20 km east of the Southern Alps' Main Divide [Avendonk et al. 2004, Davey

et al. 1998, Holbrook et al. 1996, Kleffmann et al. 1998, Scherwath et al. 2003, Smith et al. 1995, Stern 1995, Stern and McBride 1998, Stern et al. 2000, Wellman 1979, Woodward 1979]. This asymmetrical thickening of up to 17 km [Scherwath et al. 2003] is thought to be due to a *decollement* at the base of the Pacific crust, which is less resistant and therefore more deformed than the Australian crust [Avendonk et al. 2004, Beaumont et al. 1996], separating the Cretaceous oceanic lithosphere from its overriding metamorphosed sedimentary rocks. The old oceanic crust is thought to thicken with the mantle lithosphere [Stern 1995, Walcott 1998, Wellman 1979] while the overriding greywackes and schists are obducted along the Alpine fault [Davey et al. 1998, Smith et al. 1995, Walcott 1998]. The up-thrusting of lower crustal rocks results in the shoaling of the brittle-ductile transition from 15 km to 6 – 8 km depth [Norris and Cooper 1995, Walcott 1998]. Beaumont et al. [1996] suppose that the mantle lithosphere is subducting along into the asthenosphere, but teleseismic P-wave delay data suggest a uniform thickening of the mantle lithosphere rather than subduction [Stern et al. 2000]. A cold and dense zone has been suggested to lie beneath the crustal root at a depth of about 120 km [Stern et al. 2001].

Low Velocity Zone

The Low Velocity Zone (LVZ) associated with the Alpine fault is coincident with the thickened crust [Stern et al. 2001] and was first modelled by Scherwath et al. [2003] with wide-angle reflection data. At depths greater than 8 km, neither anisotropy nor the presence of unconsolidated rocks can adequately explain the LVZ and therefore, Stern et al. [2001] propose that high fluid pressure may be the cause for low seismic velocities. At shallower depths, Smith et al. [1995] suggest that mechanical processes downgrade the rocks and the low velocities are likely to be caused by faulted and strained rocks.

Uplift and denudation

The uplift rate is thought to be at least 16 mm/yr in the study area [Kleffmann 1999, Walcott 1979]. Erosion, which is a function of elevation [Wellman 1979] and of the climatic situation (glacial patterns and precipitation rates), is said to have enhanced the denudation rates of about 10 mm/yr for the Southern Alps [Blythe 1998, Tippett and Kamp 1993]. The uplift rate, as well as the topography, diminish in both the northern (Hokitika) and the southern (Haast) sections of the Southern Alps, localising the area of maximum deformation to the central South Island [Kamp and Tippett 1993, Little et al. 2005, Walcott 1998].

Glacial history

The Otira glaciation, New Zealand's Last Glacial Maximum, which reached its extremum at 18 Ka [Petit et al. 1999, Suggate 1990, Suggate and Almond 2005], and the Waimea glaciation, which culminated at 140 Ka and had greater proportion than the afore-mentioned one, were separated by the Kaihinu interglacial period (140 Ka – 100 Ka). The last glacial retreat began at 14 Ka [Suggate and Almond 2005, Sutherland et al. 2006].

1.2.2 Geology and features of the study area

Crustal terranes

The geology of the study area can be divided into two main crustal terranes:

- **Western province.** Rocks that are Precambrian to Devonian in age and were once a part of Gondwana.
- **Eastern province.** A group of rocks consisting of mainly low-grade metasediments formed during the Mesozoic. It includes the Torelesse greywackes and the Haast schists, which are being up-thrusted along the Alpine fault.

Fault related rocks

On a more local scale, apart from clastic sediments, river gravels, glacial till as well as two granitic intrusions, the rocks found in the vicinity of the Alpine fault are associated with fault zones. Three types of rocks form at three distinct depths within a fault zone [Mooney and Ginzburg 1986, Sibson 1977, Young 1968]:

- **mylonites** form at depth in a ductile regime in temperatures neighbouring 350°C. Unlike the two other types of rocks, mylonites have a foliated and cohesive structure.
- **cataclasites** result from elastico-frictional deformation usually at depths of about 4 km. They are faulted and expose a random-fabric structure.
- **fault gouge** usually form superficially or at shallow depths. They are known to be extensively deformed and faulted.

The shoaling of the brittle-ductile transition zone may result in diminishing of the formation depth of these rocks.

South Westland Basin

Convergence has formed a flexural sedimentary basin known as the South Westland Basin (SWB) [Cotton 1956, Nathan 1977]. Extending from Hokitika to Fiordland [Sircombe and Kamp 1998], the SWB is limited to the southeast by the Alpine fault and thins offshore onto the Challenger Plateau. It has been classified as a foreland basin [Harrison 1999, Sircombe and Kamp 1998] as well as a prograding deltaic basin [Beaumont et al. 1996, Walcott 1998].

Rivers

Three rivers flow onto the Whataroa River flood plain, all of which cross the Alpine fault as can be seen on figure 1.1:

- **Little Man River**, also known as Dry Creek, is a late tributary of the Whataroa River and joins the flood plain on the northeast of Whataroa.
- **Waitangitoana River** flows onto the southwest of the Whataroa township alongside the western flank of the Price Range. One of its tributaries is Gaunt Creek renowned for its Alpine fault outcrop.
- **Whataroa River**. Combining the flows of both the Whataroa River and the Perth River, this river flows onto the southeast of the township alongside the eastern flank of the Price Range.

1.3 Study strategy

Two geophysical methods are jointly used in this study:

- Gravity anomaly modelling.
- Seismic refraction ray tracing.

In chapter 2, a gravity line that runs across the Whataroa River flood plain (black circles in figure 1.2) yields depths to basement used to constrain the seismic models. In chapter 3, refraction first breaks from a seismic survey (beige inverted triangles in figure 1.2) running along the Whataroa River and crossing the afore-mentioned gravity line are processed and modelled by ray tracing. The resulting velocity structure provides an approximation of the extent of the LVZ associated with the Alpine fault in the top 8 km of the crust. In chapter 4, available gravity data (blue triangles in figure 1.2), which cross both the gravity and the seismic survey lines, are used to assess the results of the two previous applied methods. The main results are presented along with a discussion in chapter 5.

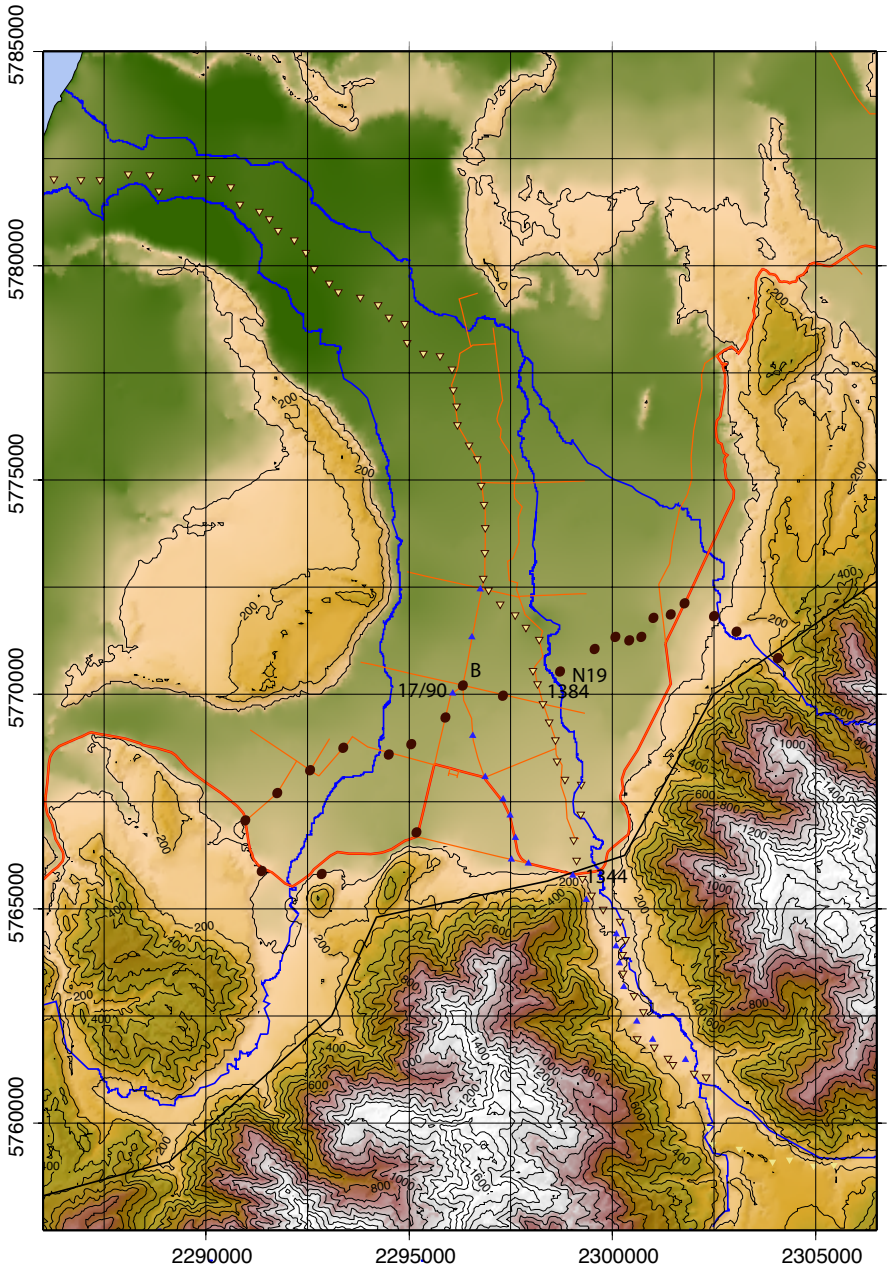

Figure 1.2: Map showing the three datasets. The stations that were occupied for the gravity profile of November 2006 (black circles) cut across the 1996 SIGHT project's receiver array (beige inverted triangles) and the GNS gravity line (blue triangles) collected in 1964. The labeled station names are at the junction with another dataset.

Chapter 2

Gravity survey of the Whataroa flood plain

2.1 Gravity Survey

The gravity survey was conducted in Whataroa during the 21 – 23^{rd} November 2006. A total of 24 stations, including an absolute gravity station and two stations of the Institute of Geological and Nuclear Sciences' (GNS) gravity network, were occupied. The stations were spread across the flood plain in a southwest-northeast direction either on the highway, on farm roads, on paddocks or on the river gravel (figure 2.1).

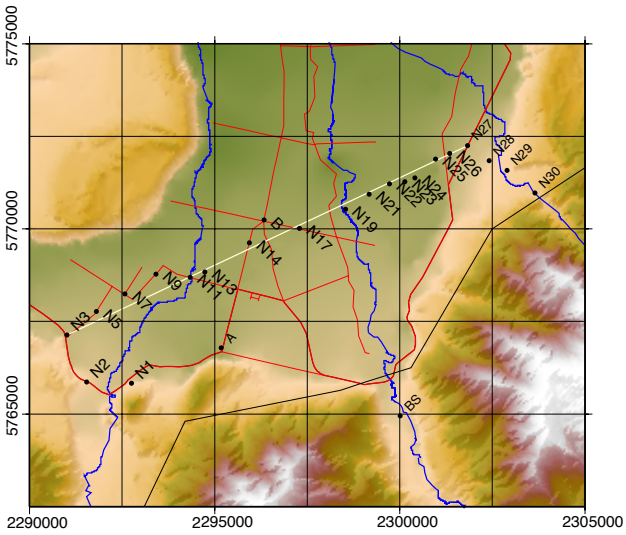

Figure 2.1: Map showing the gravity stations' positions and names. The beige line represents the intended survey line. The stations labeled 'A' and 'B' are common with the GNS gravity network. 'BS' is the Whataroa base station.

2.2 Data

The gravity measurements were done with the *Lacoste-Romberg* analog gravity meter G-179. A *Trimble* static GPS was used to calculate the station's positioning and relative height. In case the latter failed, a *Garmin* handheld GPS, a barometer and a thermometer were also used throughout the survey. At least three correct readings per station were made for each analog instrument (gravity-, baro- and thermometer) to minimise the reading errors.

A 'loop' station was re-occupied each day to determine instrumental and temporal drift (figure 2.2c). The daily drift gradients and the result of the consistency check can be seen on figure 2.2b. All the stations were linked to the Whataroa base station (figure 2.2a) whose value was used for the data reduction.

a.

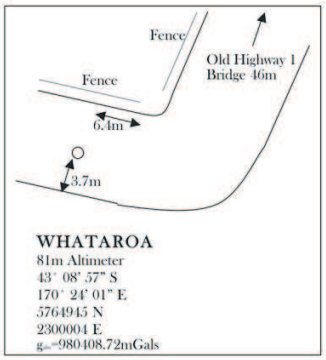

b.

Coordinates		GNS		Personal Survey	
NZMG E/N		name	reading	name	reading
2295170	5766782	17/235	5432.43	A	4083.88
2291538	5765865	17/237	5433.80	B	4085.22
Difference in mGals			1.37		1.34

c.

	Description	Time of reading decimal hours	Difference decimal hours	Readings mGals	Difference mGals	Drift rate mGals/hr
Day1	DoC Office, Franz Josef	15.41	4.18	4066.21	-0.03	-0.0067
		19.59		4066.18		
Day2	Motel Room, Franz Josef	10.89	11.03	4067.73	0.06	0.0057
		21.92		4067.80		
Day3	Station 'A', Whataroa	9.41	2.58	4083.89	0.04	0.014
		11.99		4083.92		

Figure 2.2: **a.** Information about the reference base station in Whataroa based on Roberston and Reilly [1958]. **b.** Consistency check between the two data sets showing an overall discrepancy of 0.03 mGals. **c.** Summary table of the daily loop stations and their relative temporal drift gradient.

2.2.1 Data reduction

The data were reduced using *Microsoft Excel*. The mean of the three readings, $\bar{X}$, is converted into milliGals, X_{mGal}, by the help of the gravitymeter's latest reliable calibration table (appendix A) updated by Toulmin [2006]:

$$X_{mGal} = 4005.39 + [(\bar{X} - 3800)1.055009364] \tag{2.1}$$

The readings are drift corrected, X_{corr}, for the temporal and instrumental drift, δ, as follows:

$$X_{corr} = X_{mGal} + [(t_0 - t)\delta] \tag{2.2}$$

The static shift, g_{static}, is obtained by subtracting X_{corr} at the Whataroa base station to the absolute gravity value at the same location [Roberston and Reilly 1958]. The observed gravity, g_{obs}, is thus defined by:

$$g_{obs} = g_{static} + X_{corr} \tag{2.3}$$

Hence, the anomaly is the difference between the observed value of gravity, g_{obs}, and the one predicted by an ideal Earth model, $g_{predicted}$, defined as:

$$g_{predicted} = g_{lat}^{1930} - \Delta g(h) - TC \tag{2.4}$$

The first term of the equation (2.4), g_{lat}^{1930}, is the latitude-dependent gravity value predicted by the 1930 International Gravity Formula:

$$g_{lat}^{1930} = 978049[1 + 0.0052884sin(\lambda)^2 - 0.0000059sin(2\lambda)^2] \tag{2.5}$$

with λ being the latitude at the station.

The second term of the equation (2.4), $\Delta g(h)$, is the height correction including the Bouguer plate ($2\pi G\rho h$) and the Free Air ($0.3086h$) corrections. These are combined because they are both dependent upon the height (in m), h, of the station. The height estimate from the *Trimble* static GPS survey was 31.6 m above that predicted by the GNS model of height difference with respect to the Geoid. So, to calculate $\Delta g(h)$, this value had to be subtracted from the heights obtained to give the corrected height, h_{corr}:

$$\Delta g(h) = (0.3086 - 2\pi G\rho)h_{corr} \tag{2.6}$$

where G=6.67310^{-11} m^3/kg/s^2 is the universal gravitational constant and ρ=2.67 Mg/m^3 is the assumed density for the Bouguer plate.

The third, and final, term of the equation 2.4, TC, is the terrain correction. The Hammer [1939] method was used in the field to estimate the terrain correction of the *inner zones*. The zone A (0 – 2 m) was chosen to be flat as the effect on gravity is inversely proportional to the distance from the reading point to the terrain irregularity. Estimates on the field were carried out for the Hammer zones B (2 – 16.6 m), C (16.6 – 53.5 m) and D (53.5 – 170.1 m). The values in milliGals of the terrain corrections of the immediate 170.1 m that surround the station were derived with the terrain correction table (see appendix B). The *outer zones*' terrain correction (beyond 170.1 m from reading point) have been computed with the software tool *gred.tcl* [Rob Davies 2000].

Pressure and temperature measurements were only used once in this survey to yield the relative height of station N30. The height difference, Δh, of a station with respect to a reference location of known height can be derived with their temperatures in degrees Celsius ($^\circ C$), T and T_{ref},

and the pressure in milliBars, P and P_{ref}, as described in the following equation, also known as Babinet's formula:

$$\Delta h = 16000(1 + \frac{T_{ref} - T}{500})\frac{P_{ref} - P}{P_{ref} + P} \tag{2.7}$$

Hence, the Bouguer anomaly, g_{BA}, which can be found in appendix C, is obtained as follows:

$$g_{BA} = g_{obs} - g_{predicted} \tag{2.8}$$

2.2.2 Error estimation

The height and location data, obtained from the *Trimble* static GPS, had an uncertainty of the order of 10 and 20 cm, respectively. This involves an error of the order of 6 and 0.01 μGal, respectively. The barometer has a resolution of 0.1 mBar inducing an uncertainty of 1 m and a gravity error of 0.03 mGal. The *Garmin* handheld GPS has a horizontal resolution of 15 m causing an error of 0.012 mGal.

The estimated uncertainties of the *inner zones* of the terrain correction are thought to be of 0.01 mGal for the stations on the flood plain as almost no near-station terrain irregularities were visible. However, the stations N1 – N3 and N28 – N30 were in proximity of important topographical features (Southern Alps, glacial moraines) and have an estimated uncertainty of 25%.

Difficulties were experienced to level the gravity meter during field work and may have caused unusual drift and erratic readings. All but one station were sampled by the same person which attributes a low subjectivity to the readings. The gravity meter's resolution is 0.01 units corresponding to 0.01 mGal accuracy. However, the resulting converted values have a different range of precision. The standard deviation in the reading ranged from 0.02 – 0.36 mGal, the average being of 0.1 mGal. The standard deviation, σ, represents the mean difference of each individual reading, x_i, with respect to its mean value, $\bar{x}$. The equation is as follows:

$$\sigma = \sqrt{\frac{\sum_{i=1}^{N}(x_i - \bar{x})^2}{N}} \tag{2.9}$$

Model uncertainties are difficult to estimate but may come from the fact that a non 2-D array is treated and modelled as two-dimensional. The horizontal resolution of the model might therefore be decreased.

The non-uniqueness of the result, which is inherent to forward modelling methods [Zelt 1999], is also to be kept in mind.

Finally, as mentioned by Kleffmann [1999], the total uncertainty for each station is determined by using the quadratic sum of all the different contributing parts [Taylor 1982]. The different sources of error and their attributed uncertainty are summarised in table 2.1.

Station	*Height*	*Location*	*Terr. Corr.*	*St Dev*	*Quad. Sum*
N1	0.006	0.0001	0.25	0.04	0.25
N2	0.006	0.0001	0.25	0.08	0.26
N3	0.006	0.0001	0.25	0.09	0.27
N5	0.006	0.0001	0.01	0.14	0.14
N7	0.006	0.0001	0.01	0.11	0.11
N9	0.006	0.0001	0.01	0.23	0.23
N11	0.006	0.0001	0.01	0.36	0.36
N13	0.006	0.0001	0.01	0.02	0.02
N14	0.006	0.0001	0.01	0.08	0.08
B	0.006	0.0001	0.01	0.12	0.12
N17	0.006	0.0001	0.01	0.02	0.02
N19	0.006	0.0001	0.01	0.05	0.05
N21	0.006	0.0001	0.01	0.23	0.23
N22	0.006	0.0001	0.01	0.08	0.08
N23	0.006	0.0001	0.01	0.07	0.07
N24	0.006	0.0001	0.01	0.04	0.05
N25	0.006	0.0001	0.01	0.07	0.07
N26	0.006	0.0001	0.01	0.03	0.03
N27	0.006	0.0001	0.01	0.15	0.15
N28	0.006	0.0001	0.25	0.06	0.26
N29	0.006	0.0001	0.25	0.01	0.25
N30	0.038	0.0120	0.25	0.12	0.28

Table 2.1: Table of the estimated ± error in mGals for each data collecting process, for each station and the total uncertainty for each station. Terr. Corr.: terrain correction, St. Dev.: Standard Deviation, Quad. Sum: Quadratic Sum.

2.2.3 Regional gradient

To model the shallow structures the effect on gravity of lithospheric processes, such as the crustal thickening, need to be removed by determining and subtracting the regional gravity field from the observed gravity data. The complexity of the regional gradient in this region made that we could not determine it on a map. Therefore, the model proposed by Stern et al. [2000], displaying a thickened mantle and a 34-km-thick crust, is used to determine the regional gradient (figure 2.3a).

As can be seen on figure 2.3b, the regional trend over the study area (close-up in figure 2.3c) is approximately linear and is closely fitted by a line of equation:

$$y = -1.2685x + 0.7848 \tag{2.10}$$

The regional trend, ϑ, which reaches more positive values towards the northwest is of 1.2685 mGal/km. To correct for the regional gradient, all the stations were projected onto the intended survey line (beige line in figure 2.1). The result, found in appendix D, is a regionally corrected Bouguer anomaly, BA:

$$BA = g_{BA} - (\vartheta \times d) \tag{2.11}$$

where d is the offset from the station to the line.

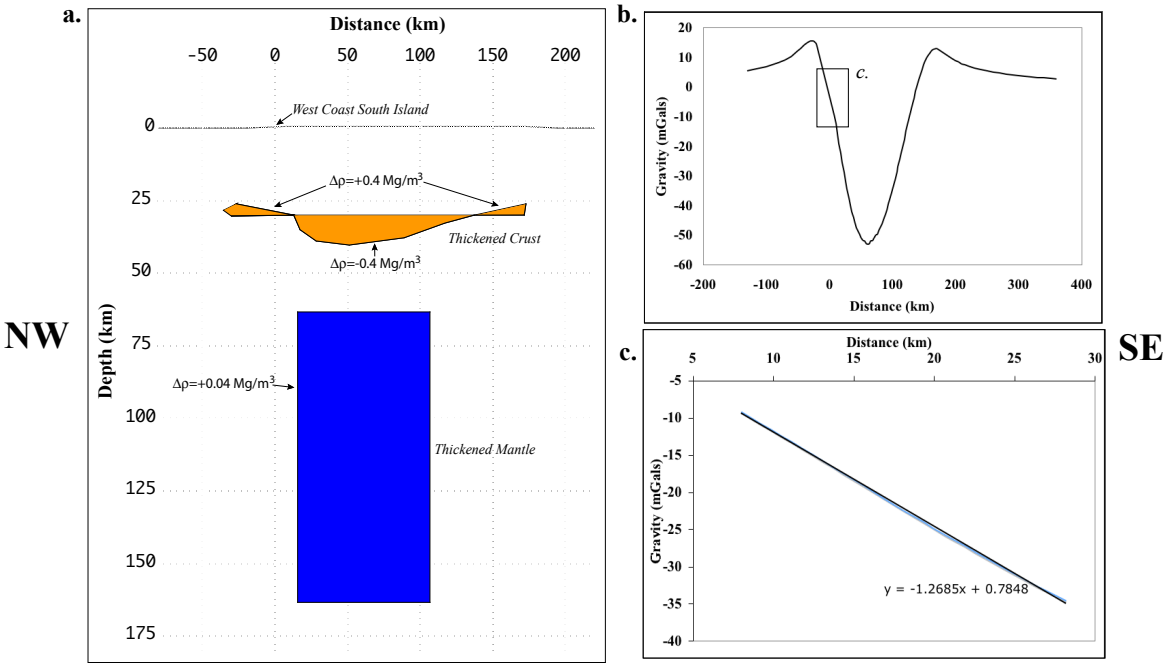

Figure 2.3: **a.** The gravity model proposed by Stern et al. [2000] showing both the crustal and mantle thickening. The two orange cones represent where mantle material replaced the crust causing a positive density contrast of +0.4 Mg/m^3. The central orange body represents the intrusion of crustal material into the mantle causing a negative density contrast of -0.4 Mg/m^3. The blue rectangle represents the asymmetrically thickened mantle with a density that is 0.03 Mg/m^3 greater than the surrounding mantle. **b.** Plot of the gravity anomaly caused by the gravity model. The rectangle represents the gravity anomaly's variation within the study area. **c.** Close-up of the gravity anomaly in the study area. The straight line of equation $y = -1.2685x + 0.7848$ closely fits the curve. The regional gradient is of ϑ=+1.2685 mGal/km towards the northwest.

2.3 Densities

The dominant basement geology of the west of the Alpine fault, whose geometry is expected to be relatively unfaulted [Sircombe and Kamp 1998], has an estimated density of 2.67 Mg/m^3 [Hatherton and Leopard 1964]. We made the assumption that we should only find sediments overlying the basement as most stations were in the flood plain well away from the Alpine fault. River gravels, clastic sediments, and glacial till, which are found by Langdale and Stern [1998] to have thicknesses of 500 – 1600 m on the east of the South Island, have an average density of 2.20 Mg/m^3, hence causing a negative contrast of -0.47 Mg/m^3.

2.4 Model

The data were modelled in *Grav2D*. The value of gravity of the two basement stations were subtracted to the data in *Grav2D* to take away the remaining gravity trend. The resulting model is presented in figure 2.4b and the fit of the calculated gravity anomalies to the observed ones is shown on figure 2.4a.

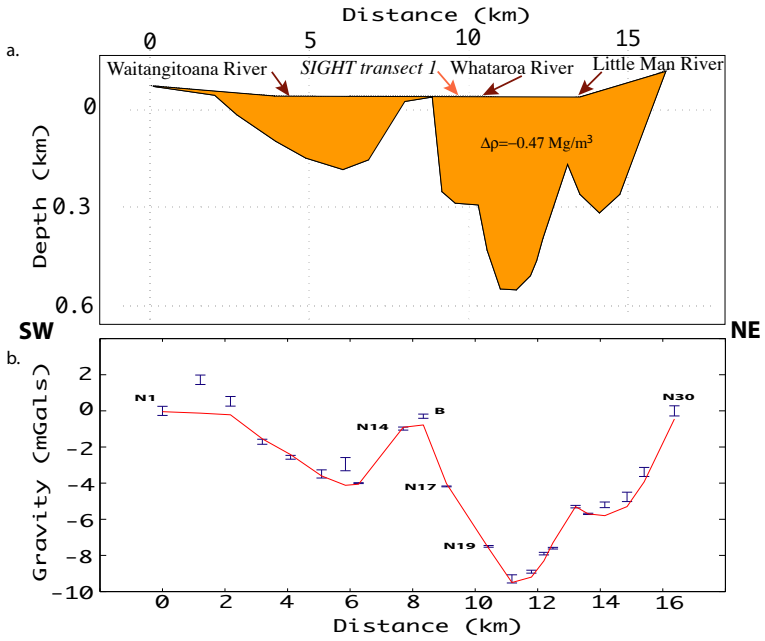

Figure 2.4: **a.** The gravity model with the orange body representing the sediments with a negative density contrast of -0.47 Mg/m^3. This figure has a 10x vertical exaggeration. **b.** Plot of the fit of the observed gravity anomalies (blue dots), with their individual error bounds, to the calculated ones (solid red line).

2.5 Conclusions of the gravity survey

1. Depth to basement:
    - 150 m under the Waitangitoana River
    - 250 m under the Little Man River
    - 300 m under the Whataroa River with a trough reaching 550 m depth 1 km northeast of the river.
2. The buried erosion valleys of the three main rivers have kept their glacial shape.

Chapter 3

Seismic Refraction Survey

3.1 SIGHT

3.1.1 SIGHT - the project

The South Island Geophysical Transect (SIGHT) project was a joint undertaking from United States and New Zealand scientists carried out during the first months of the year 1996. Its aim was to investigate the South Island's continental collision zone at depth. Although the data collection campaigns span the whole of the South Island, the main area of focus was its central part, where the narrowness is highly favourable to onshore-offshore seismic data acquisition across the plate boundary [Okaya et al. 2002]. The geophysical methods involved in this large scale campaign were mainly controlled seismic source and magneto-telluric, with the seismic work carried out onshore and offshore of the South Island. The seismic experiments produced four complementary data sets:

- land shots recorded onshore by land receivers
- offshore air-gun shots recorded:
  - onshore by land receivers
  - offshore by Ocean Bottom Seismometers
  - offshore by a streamer array

Serendipitous teleseismic events from the western Pacific region were recorded and enabled the modelling of the lithospheric thickening by Stern et al. [2000].

On land, two, 50-km-apart, northwest-southeast-orientated seismic transects were designed to cross the central South Island from the Canterbury Basin over the Southern Alps to the West Coast, perpendicular to the plate boundary. These land transects were projected offshore towards the Tasman Sea and the Pacific Ocean where the scientific vessel R/W Ewing fired various airgun lines to complete the seismic array [Scherwath et al. 1996].

3.1.2 Transect 1

The deployment of the land Transect 1, north of Transect 2, approximately follows the Rangitata River valley, across the Main Divide and down the Whataroa River valley. The receiver array consisted of 400 one-to-three component instruments with a nominal spacing of 400 m. Two different types of instruments were used to record the data:

1. The REFTEKs have a natural period of 4.5 Hz with a sampling rate of 4 ms and have their three component motion sensors lodged in the same casing.

2. The EDAs, only used for land shot data collection, have a natural frequency of 2 Hz, sample every 8.3 ms and have a separate housing for each sensor.

Each instrument was buried at a depth of about 30 – 50 cm or at least covered with soil to maximise the coupling. The receivers were orientated parallel to the main line and the radial component had an azimuth of 298° from the magnetic north. The timing of the instruments was done either by integrated GPS clock, by time "pulsing" with synchronised programmable palm-top computers or by integrated synchronised clocks.

A total of 16 shots, with detonation charges ranging from 50 to over 1200 kg, exploded during the nights of the 27 – 29^{th} of January 1996 in order to minimise environmental background noise. The data recorded by the EDAs were resampled for the sampling rate to match that of the REFTEKs and the 90 seconds long traces were then stored in SEG-Y format.

3.2 Data

The dataset for this seismic study consists of the traces of the vertical components of 76 instruments (receiver number 1252 – 1552 both EDAs and REFTEKs) of four shot gathers (Shot Point (SP) 13 – 16) shown in figure 3.1. The details of the four shots used in this study are given in the table 3.1.

Shot number	*Location*	*Height*	*Depth to top of charge*	*Charge size*	*Time (UTC)*
		MASL	*Metres*	*Kg*	*yy:ddd:hr:mn:ss.dec*
13	**Nolans Hut**	**181**	**-**	**50**	**96:028:23:00:01.366**
14	**Whataroa**	**65**	**25.1**	**291.7**	**96:027:14:30:00.002**
15	**Adamson Rd**	**20**	**28.8**	**781.7**	**96:027:13:00:00.001**
16	**West Coast**	**10**	**45.1**	**1206.7**	**96:027:12:00:00.001**

Table 3.1: Shot information of SP13, SP14, SP15 and SP16.

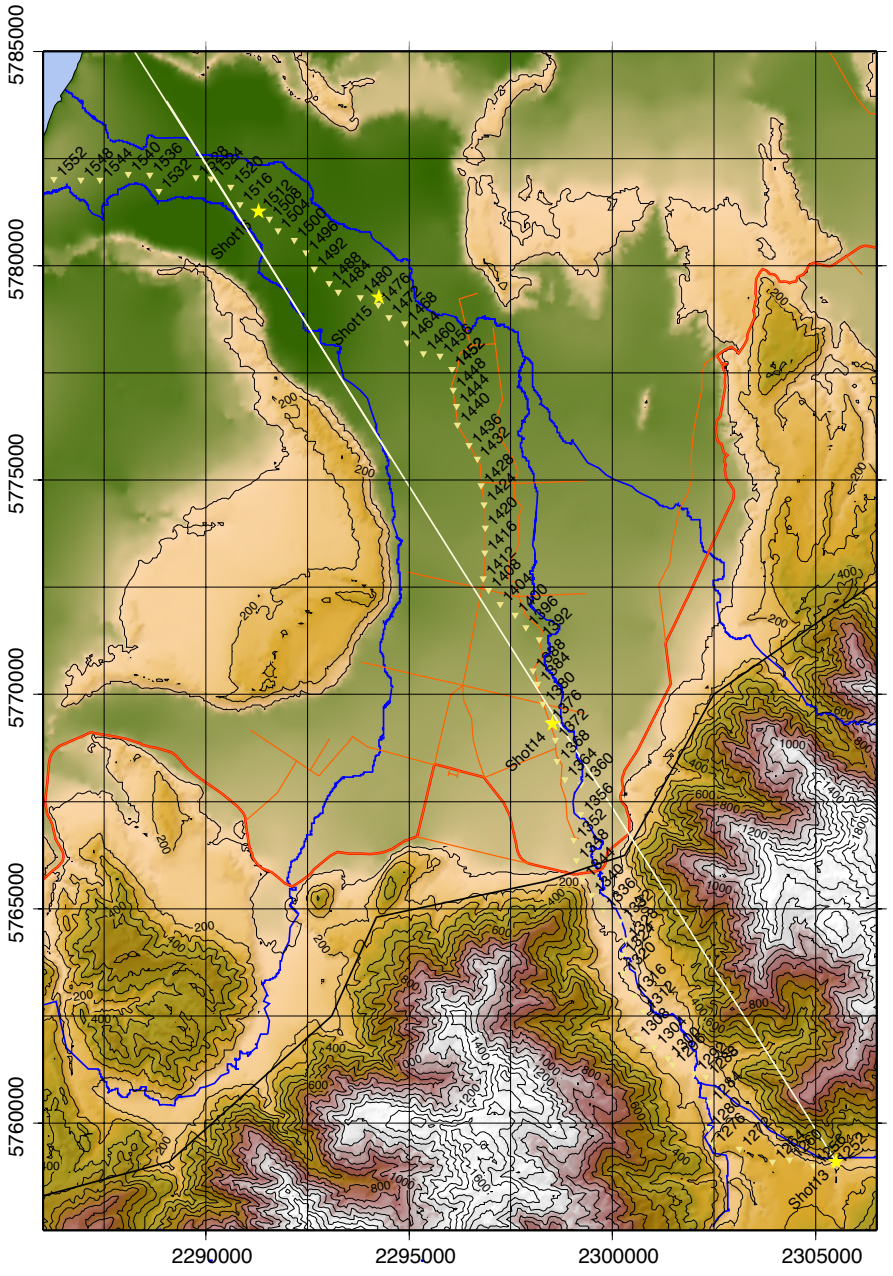

Figure 3.1: Map of the shots' (yellow stars) and receiver array's location (beige inverted triangle) along the Whataroa River valley. The receivers and the shot points were projected onto the white line for the modelling. The approximate position of the Alpine fault's surface trace is represented by the thin black line.

3.2.1 Data processing

Processing sequence

The data were processed with GLOBE *CLARITAS*. The dead and noisy traces were muted but no surgical mute was applied. The data were debiased over the whole length of the traces. A frequency filter (figure 3.2) was applied to segregate and discard the signals of undesired frequencies. The first arrivals were estimated to be at a frequency of 15 – 20 Hz.

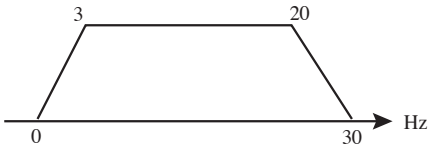

Figure 3.2: The frequency filter applied to the seismic data.

Furthermore, the data had their amplitudes balanced and averaged over the whole trace and an Automatic Gain Control (AGC), with a window of 2000 ms, was applied. The first breaks, whose travel times were reduced by 6 km/s, were picked manually on the *'sqc'* console of *CLARITAS*.

Reciprocal travel times

Assuming that the Earth's structure did not change during the experiment, the travel times, when the location of a receiver and a shot point is interchanged, should be equal. If these are not reciprocal, a verification of the picking method and of the receiver's offset calculation should be considered [Sjögren 1984]. The plot in figure 3.3 shows that the travel times of the first arrivals of the four shots are reciprocal.

Data preparation for modelling

For the continuity of the model, the 76 receivers were projected onto a common line (white line in figure 3.1), centered at SP13 (x_0, y_0), with an approximated azimuth of $\alpha \simeq 328°$. The offset, d, of each point (x, y) to the reference line is:

$$d = -(x - x_0)sin\alpha + (y - y_0)cos\alpha \tag{3.1}$$

The relative offset to SP13, the time delay and the first apparent-velocity analysis for each shot are summarised in table 3.2. The picks files are exposed with their respective processed shot gather in the appendix E.

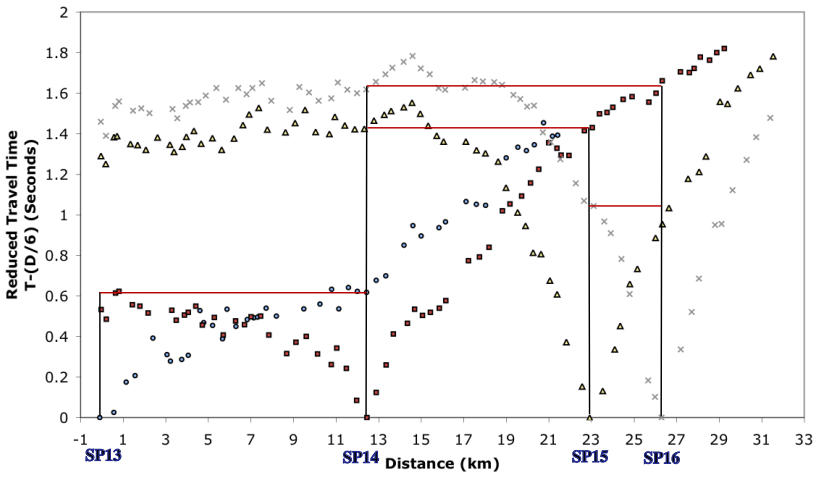

Figure 3.3: This plot displays the position and the first arrivals of SP13 (blue circles), SP14 (red squares), SP15 (yellow triangles) and SP16 (crosses). The black vertical line are the projection of the shot's position along the array and the red horizontal lines between them shows that the travel times are reciprocal within the the range of variability.

	Offset from SP13	*Static shift*	*First Apparent Velocity Analysis for estimated layers (values are in km.s^{-1})*							
			1		*2*		*3*		*4*	
Shot Point	*(km)*	*(ms)*	*E*	*W*	*E*	*W*	*E*	*W*	*E*	*W*
13	0	-5332	X	2.3	1.5	1.5	1	1	1	1
14	12.36	-5093	X	12.4	13.3	2.5	1.4	1.4	1.7	1.7
15	23.08	-4968	X	23.3	X	3.3	6	2	8	1
16	26.32	-5034	X	6.2	X	5.4	26.5	X	25.3	X

Table 3.2: Table showing the relative offsets from SP13, the time delay (between the turning-on of the instrument and when the shot detonated) and the first apparent velocity analysis. The 'X' notices that no velocity estimate of the specific layer could be made.

3.2.2 Error estimation

Data acquisition

Even though they were buried, the signal to noise ratio is decreased because the instruments recorded the continuous humming of the near-by river, which is significantly greater on steep slopes and during the summer months. This should, however, not matter for shots of large charge size.

With only 50 kg of charge size, up to 24 times smaller than the other shots, SP13 detonated at the surface (in the river) thereby decreasing the signal to noise ratio. The shot gather of SP13 has its northwestern part dominated by noise (see appendix E.1) and 24 traces could not be picked. The burial depth and the inaccuracy of the receiver's clock are likely causes of uncertainty whose values are difficult to estimate.

Model

Apart from the estimated 25 ms error attributed to the manual picking of the first breaks, there is also a possibility of misidentification of the first breaks. The two-dimensional model is made from a curved receiver array and the location of the geological features may therefore be misinterpreted. The ray coverage only reaches about 4 km depth and so structures deeper than this are not claimed to be well constrained.

Although phenomena such as anisotropy and waveguiding are expected as possible causes of seismic velocity modification (section 3.3), the modelling software does not account for them. However, the depth of the charges have been accounted for in the modelling. The high frequency 'wobbles' observed on the picks are assumed to be the result of near-surface structures, which are difficult to model at this scale.

Other considerations

Ray-tracing forward modelling assumes the geometric ray theory, whose rapid result is a good approximation of the structure. However, the ray theory does not directly provide information about the wave amplitudes and frequencies, it only gives us the travel times of the rays [Stein and Wysession 2003].

3.3 Constraints

Seismic velocities

The velocity constraints found in the literature are to be found in the table 3.3.

Rocks	*Velocity*	*Reference*
Basement gwke & sch	5 - 6 km/s	Davey et al. 1998, Garrick and Hatherton 1973, Kleffman 1999 Melhuish et al. 2005, Scherwath et al. 2003, Smith et al. 1995
Alpine schist Towards AF	5.3 - 3.2 km/s	Garrick and Hatherton 1973
Sch-derived Mylonites	5.5 - 6 km/s	Garrick and Hatherton 1973
Granitic Intrusion	4.7 km/s	Garrick and Hatherton 1973
Fault gouge Cataclasite	3.4 km/s	Garrick and Hatherton 1973
Tertiary Sediments	2.3 - 3.5 km/s	Kleffman 1999
Glacial Sediments	1.7 - 2.5 km/s	Kleffman 1999

Table 3.3: Table of the velocity constraints found in the literature. In addition, a 50 – 100 m thick layer of material with a velocity of 1.6 – 1.8 km/s is placed at the surface to compensate for surface effects. gwke=greywacke, sch=schist and AF=Alpine fault.

Causes of velocity variations

Two causes of velocity variation can be thought of:

1. **Anisotropy** may be observed in a media with important fracturing and/or foliation [Smith et al. 1995, Stein and Wysession 2003, Stern and McBride 1998]:
   - The magnitude of seismic velocity reduction is proportional to the level of fracturing. For example, the formation of fault gouge reduces the protolith's seismic velocity by 20% [Eberhart-Phillips 1995].
   - The foliation of mylonites and of granitic gneisses (figure 3.4), and the important schistosity of the high grade Haast schists are likely causes for anisotropy. The Haast schists are thought to have an anisotropy of 17% [Okaya et al. 1995].
2. Seismic rays can be affected by **Wave-guiding**, a phenomenon caused by foliated structures or the presence of a LVZ, which redirects rays in a preferred direction.

Figure 3.4: Photography of a rock sample of the granitic intrusion east of Ralfes Knob presenting important foliation. Its wet density is 2.66 Mg/m^3. Each division is 1 cm wide. *Courtesy of Mark Rattenbury.*

Expected geology

Except for the obvious Pleistocene sediments (glacial till, river gravel), the expectations are to find cracked and fractured rocks adjacent to the Alpine fault as well as an important amount of fault gouge and random-fabric cataclasites at the surface as suggested by Sibson [1977], Mooney and Ginzburg [1986]. Furthermore a 1 km-thick layer of schist derived mylonites is exposed at the surface and probably might thicken at depth [Norris and Cooper 1995].

Depth to basement

A depth to basement of about 250 m is assumed from the gravity survey about 13.5 km northwest from SP13.

3.4 Models

The refraction first breaks were modeled in *MacRay*. The figure 3.5 is the general velocity structure of the shallow part of the Alpine fault that is accepted by forward modelling the four shot gathers. There is, however a 5% discrepancy between shots with rays incoming from the northwest (SP14 – SP16) and those with rays incoming from the southeast (SP13). The seismic

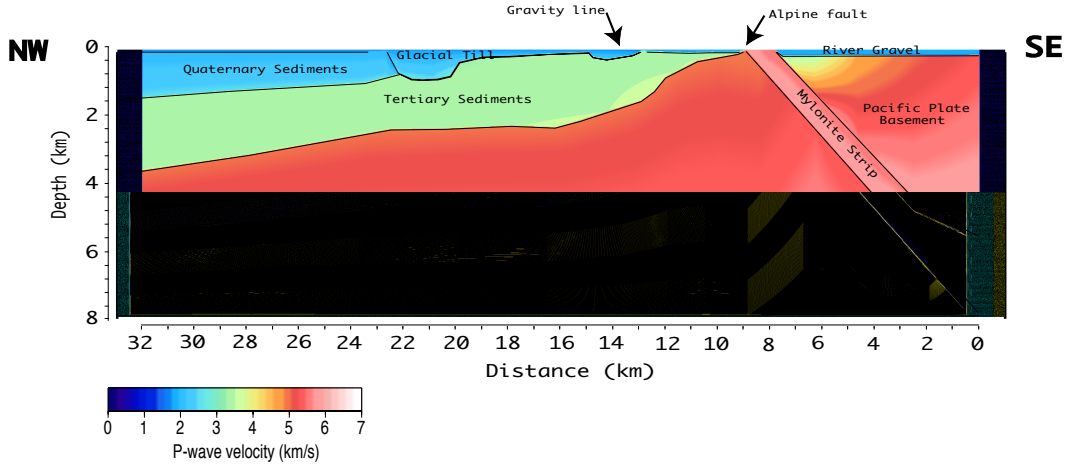

Figure 3.5: This is the velocity/geological structure that is accepted for all the shot gathers. A 5% seismic velocity discrepancy is noticed for the area to the southeast of the mylonite strip between the model of SP13 and the others.

models met the gravity constraints and coincided in the presence of:

- the **mylonite strip** which lies immediately to the southeast of the ramp of the Alpine fault;
- the **LVZ** to the southeast of the Alpine fault's surface trace;
- two **concave cavities** apparently dug out in the Quaternary and [art of the Tertiary sediments;
- and the relatively unfaulted Tertiary and Quaternary **sediments thickening** towards the sea.

The following four figures are the resulting ray-tracing models, with distances relative to SP13 and increasing towards towards the northwest. The top plots (figures 3.6a – 3.9a) show the fit of the calculated travel times (red line) to the observed ones (black dots) as a result of the propagation of the seismic rays through the velocity structure proposed by the modelled velocity structure (figures 3.6b – 3.9b). The dashed red line is to show what the calculated travel times would be if the area southeast of the Alpine fault would have the alternative velocity trend (slower for SP14 – SP16, faster for SP13).

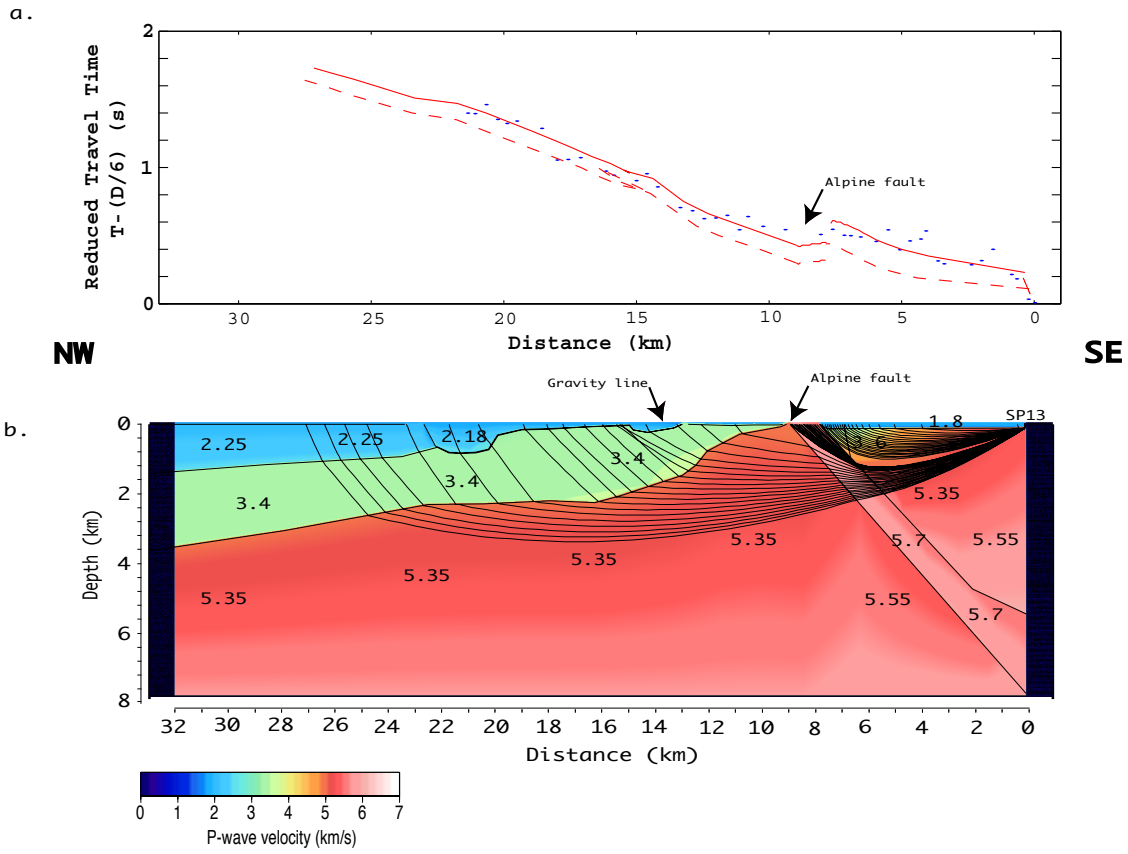

Figure 3.6: **a.** Plot of the fit of the calculated travel times (red solid line) to the observed first arrivals (blue dots) for SP13. The red dashed line show what the calculated travel times would be with faster velocities on the southeast of the mylonite strip as modelled for SP14 – SP16. The position of the Alpine fault's surface trace is indicated. **b.** This is the modelled velocity structure for SP13 along with its colour code. The position of the Shot Point (SP13) is labeled as well as that where the gravity line crosses the seismic array. The Alpine fault's surface trace and the main characteristic velocities are also indicated.

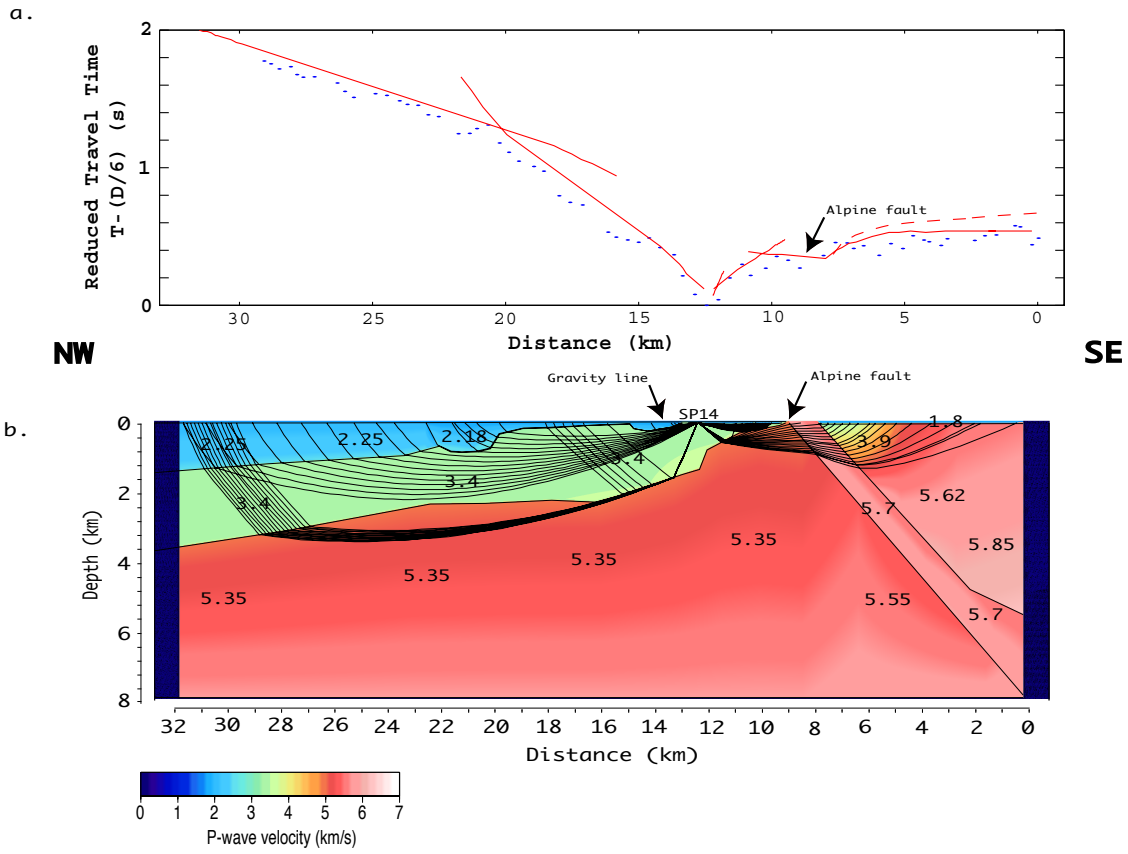

Figure 3.7: **a.** Plot of the fit of the calculated travel times (red solid line) to the observed first arrivals (blue dots) for SP14. The red dashed line show what the calculated travel times would be with slower velocities on the southeast of the mylonite strip as modelled for SP13. The position of the Alpine fault's surface trace is indicated. **b.** This is the modelled velocity structure for SP14 along with its colour code. The position of the Shot Point (SP14) is labeled as well as that where the gravity line crosses the seismic array. The Alpine fault's surface trace and the main characteristic velocities are also indicated.

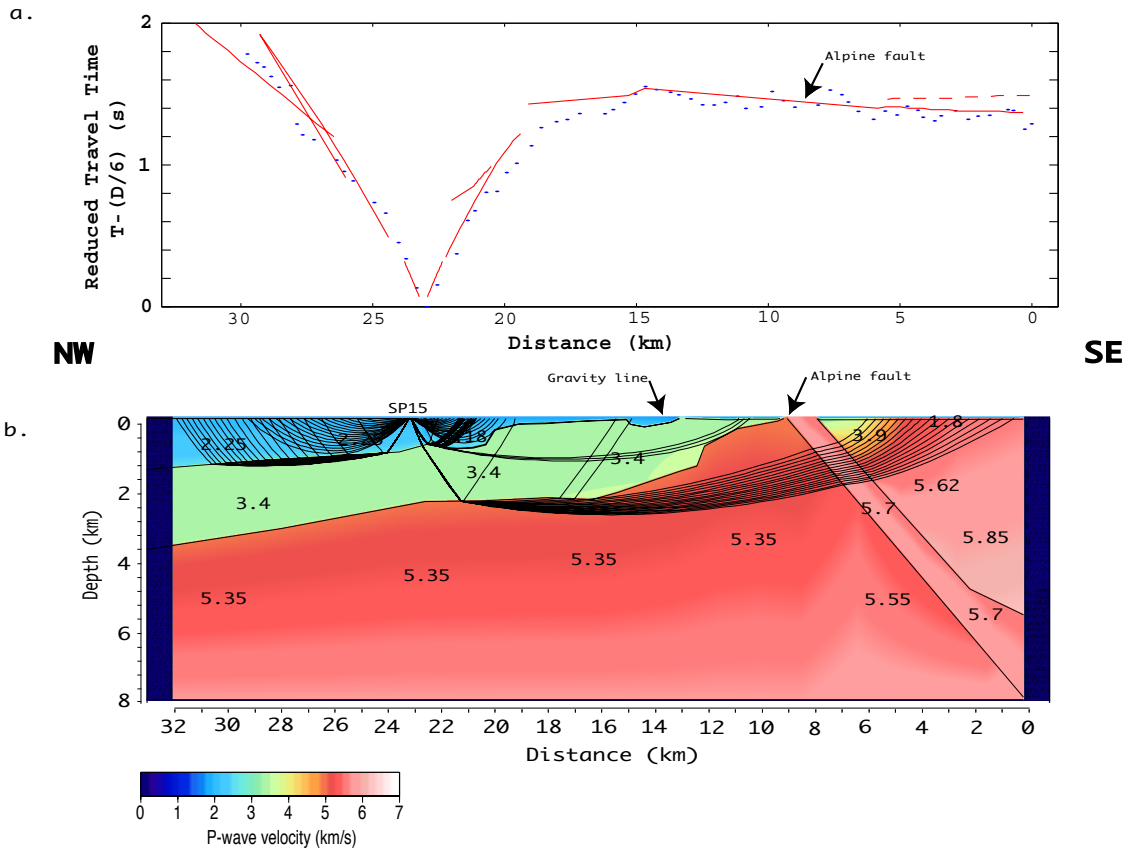

Figure 3.8: **a.** Plot of the fit of the calculated travel times (red solid line) to the observed first arrivals (blue dots) for SP15. The red dashed line show what the calculated travel times would be with slower velocities on the southeast of the mylonite strip as modelled for SP13. The position of the Alpine fault's surface trace is indicated. **b.** This is the modelled velocity structure for SP15 along with its colour code. The position of the Shot Point (SP15) is labeled as well as that where the gravity line crosses the seismic array. The Alpine fault's surface trace and the main characteristic velocities are also indicated.

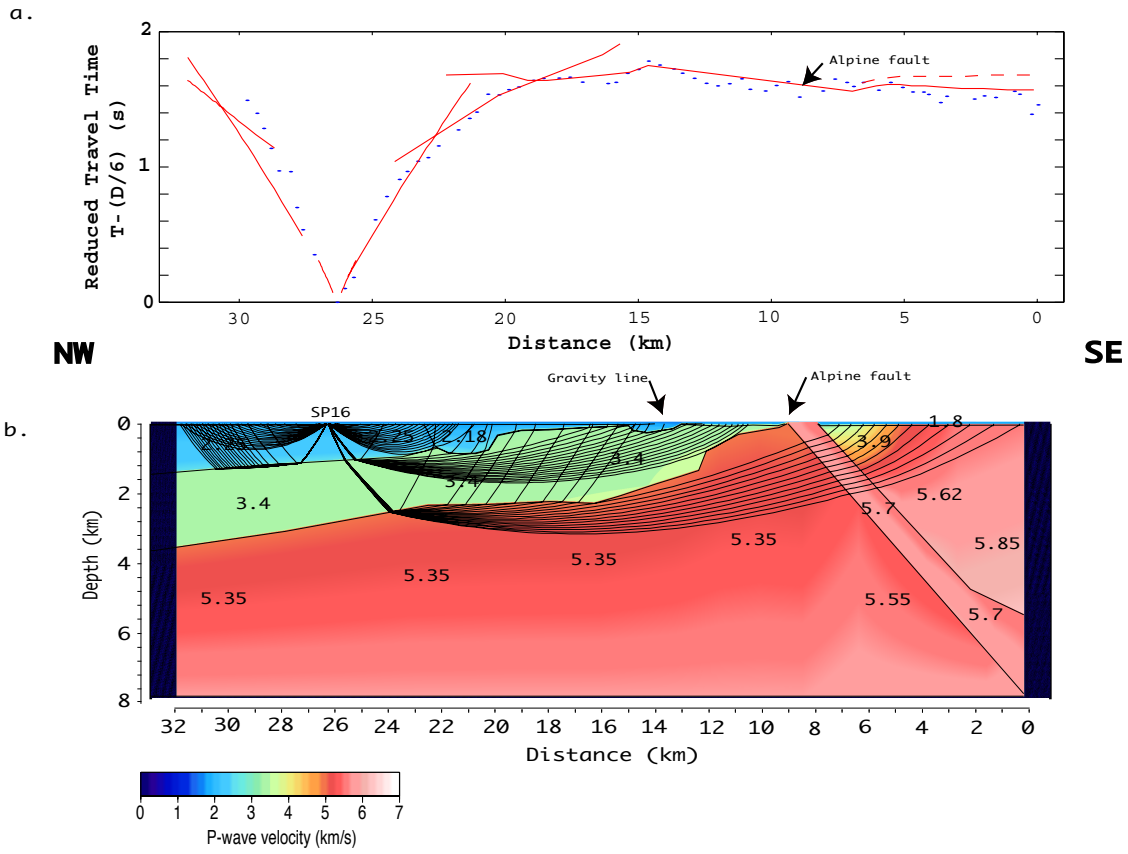

Figure 3.9: **a.** Plot of the fit of the calculated travel times (red solid line) to the observed first arrivals (blue dots) for SP16. The red dashed line show what the calculated travel times would be with slower velocities on the southeast of the mylonite strip as modelled for SP13. The position of the Alpine fault's surface trace is indicated. **b.** This is the modelled velocity structure for SP16 along with its colour code. The position of the Shot Point (SP16) is labeled as well as that where the gravity line crosses the seismic array. The Alpine fault's surface trace and the main characteristic velocities are also indicated.

3.5 Conclusions of the seismic refraction survey

1. The Alpine fault is dipping at an angle of about 50° in the top 8 km of the crust.
2. The seismic velocities of the Haast schists decrease from 5.3 km/s 9 km southeast of the Alpine fault's surface trace to 3.8 km/s immediately adjacent to the mylonite strip.
3. To the northwest of the Alpine fault, the Australian plate's basement appears relatively unfaulted and has seismic velocities that vary from 5 km/s superficially to 6 km/s at depth.
4. 5% velocity discrepancy in the area southeast of Alpine fault.
5. 3.5 km to the northeast of the river mouth are two successive concave cavities over an area of 10 – 12 km long filled with up to 600 m of material with similar velocity than glacial till.
6. The base of the Quaternary and Tertiary sediments seem relatively unperturbed.
7. The sediments of the South Westland Basin reach a thickness of about 3.5 km at the coast.

Chapter 4

GNS Gravity Database

Available gravity data from the GNS database collected between 1953 and 1975 are included in this study in an attempt to assess the results from the chapters 2 and 3. The data, in conjunction with that of the gravity line in chapter 2, were analysed two different ways:

- A map of residual gravity was produced to verify the supposed basement structures.
- A gravity line, running parallel to the seismic line and across the first gravity line, will assess whether the geological structure suggested in the seismic models in chapter 3 is realistic.

4.1 Residual gravity

Data

The GNS gravity database has a scattered coverage of the Whataroa River flood plain, with less than 0.15 station per square kilometer. A total of 47 stations, 25 of which are from the GNS network (see appendix F) and 22 from the gravity survey studied in chapter 2, are used to compute the residual gravity map (figure 4.1).

Regional correction

The data were regionally corrected by considering a line from the basement station N30 (yellow line in figure 4.1) and extending it roughly parallel to the Alpine fault and applying the regional gravity trend of 1.2685 mGal/km towards the northwest, as determined in section 2.2.3.

The azimuth of the line was determined by assuming that, in this area, the regional gravity trend's variations are approximately equal in a direction parallel to the Alpine fault's surface trace.

Considerations

For consistency between the two data sets, the terrain correction of the *outer zones* of the GNS stations were computed once again with *gred.tcl* [Davies 2002]. The mean difference was found to be of 0.33 mGal which is in the range of variability.

Only the station to the northwest of the yellow line in figure 4.1 were considered as the purpose of this analysis to map the basement features of the flood plain and not that of the river valley.

Residual gravity map

The residual gravity map was computed with *GMT 4.1.3.* by using the *blockmean* and *surface* commands to fit a surface to the values of residual gravity. Instead of a coloured surface, isogals were used to image the residual anomaly across the study area as the position of the residual gravity anomalies relative to the landmarks are essential to consider. The main finding of this analysis is stated in section 4.3.

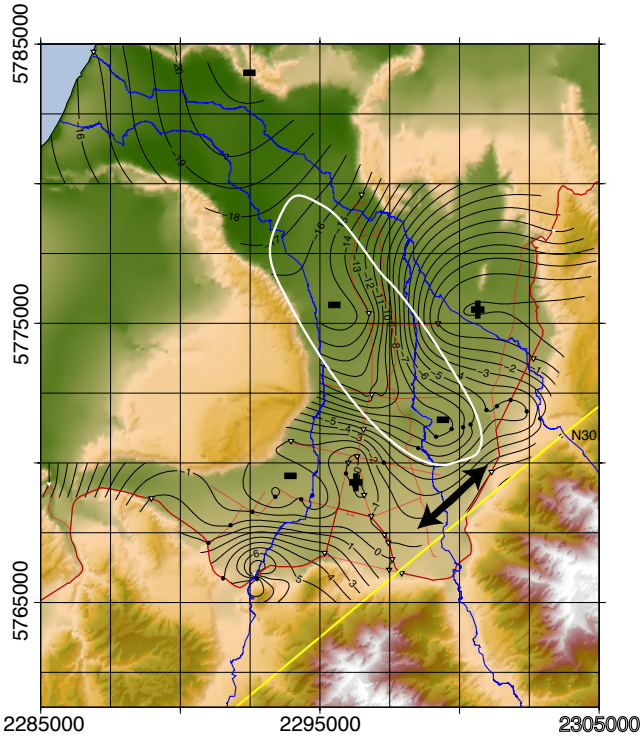

Figure 4.1: Residual gravity map of the Whataroa River food plain with the GNS network stations (white inverted triangles) and those from the gravity survey from chapter 2 (black dots). The yellow line passing through N30, striking roughly parallel to the Alpine fault's surface trace, was used to remove the regional trend from the data. The white outline delimits an apparent continuity in the residual gravity field which is offset by more than 3 km (black double-headed arrow) with the Whataroa River mouth.

4.2 Additional gravity line

Data

The data of an 18-stations gravity line were used to produce the gravity model. The gravity line follows the Whataroa River 3 km upstream from the Highway 6 and extend another 3 km downstream across the Whataroa township in a southeast-northwest direction (figure 4.2).

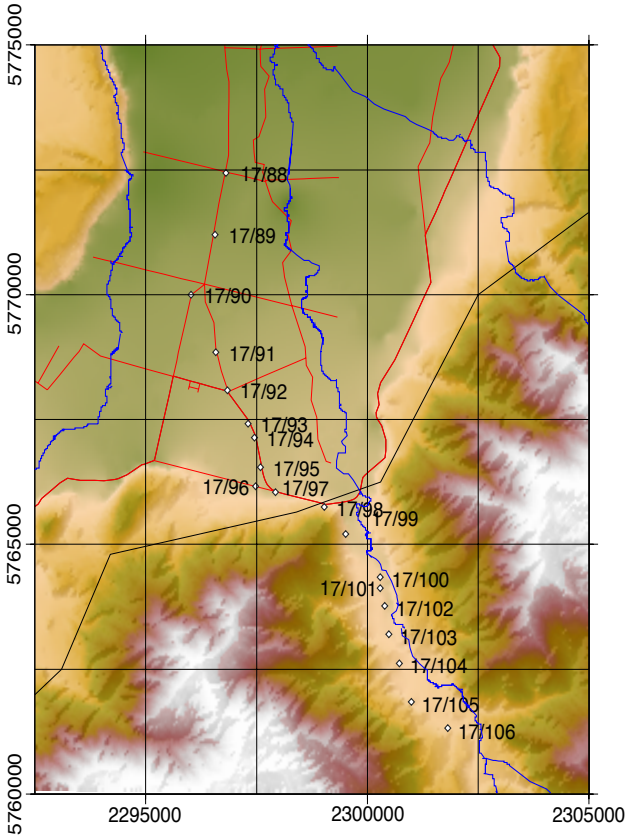

Figure 4.2: Map of the names and locations of the GNS gravity database's stations used in this analysis. The thin black line represents the approximate location of the Alpine fault's surface trace.

Regional correction

The regionally corrected gravity anomalies are equal to the difference between the Bouguer anomalies and the regional trend assumed to be linear over the study area with an equation of:

$$y = -1.2685x + 0.7848 \tag{4.1}$$

Densities

The background density is still assumed to be of 2.67 Mg/m^3. The Tertiary sediments and Quaternary sediments have been modelled with a density of 2.55 Mg/m^3 and 2.28 Mg/m^3, respectively. Glacial till, Pleistocene river gravels and mylonites have densities of 2.10 Mg/m^3, 1.90 Mg/m^3 and 2.72 Mg/m^3, respectively. The wet density of a sample of granitic gneiss (figure 3.4) from the granitic intrusion east of Ralfes Knob was determined to be of the order of 2.66 Mg/m^3. The wet density of the sample was determined as follows:

$$\rho = m/v \tag{4.2}$$

with m being the wet mass (in Mg) of the sample and v being the volume of water (in m^3) displaced by the sample.

Other considerations

The depth to basement of the first gravity line was considered. The model is not well constrained as only one station is at close proximity of basement rock (station number 17/106). We have no constraints on the geometry of the South Westland Basin other than the maximum sediment thickness is of 4 km.

Model

The data were modelled in *Grav2D*. The resulting model as well as the fit to the data are shown in figure 4.3. The finding of this analysis is in section 4.3.

4.3 Conclusions

- The residual map shows the presence of a southeast-northwest-orientated, 10 – 12-km-long, 2 – 3-km-wide negative residual gravity anomaly continuity starting 3 – 4 km to the northwest of the river mouth of the Whataroa River. It seems to have a double gradational character in that it presents two negative minima.
- The additional gravity survey accepted the presence of bodies similar in dimensions and density to those proposed in the seismic models.

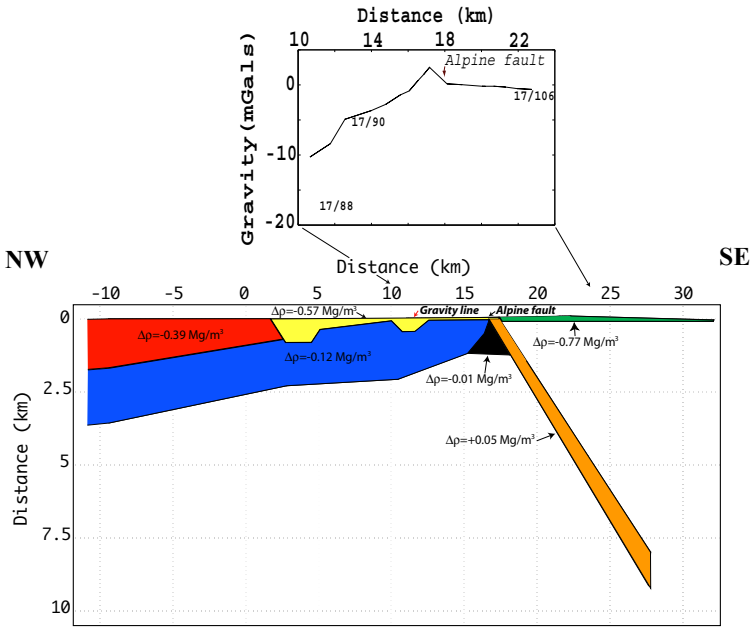

Figure 4.3: The top plot shows the fit of the calculated curve (red line) to the regionally corrected gravity anomalies (black dots). Below it is the Grav2D model of the gravity line. The green, orange and black bodies represent the Pleistocene river gravels, the mylonite strip and the granitic intrusion, respectively. The yellow, red and blue bodies represent glacial till, Quaternary and Tertiary sediments, respectively.

Chapter 5

Discussion and Conclusions

The two main findings of this thesis are:

1. Low Velocity Zone (LVZ) to the southeast and unfaulted basement geometry to the northwest of the Alpine fault.

2. Evidence of a glacial overdeepings and beheaded river mouth to the northwest of the Alpine fault.

5.1 LVZ and basement geometry

5.1.1 Major Fault model

Conceptual model for major faults

Sibson [1977] suggests that major dip-slip fault zones consist of two layers, where the first has elastico-frictional and brittle behaviours that generate random fabrics fault rocks such as fault gouge and cataclasites. The underlying second one has a ductile regime produces foliated mylonitic rocks (figure 5.1). The separation between those two layers is the brittle-ductile transition which usually corresponds to the 350°C isotherm. Depending on the convergence rates as well as the water saturation of the rock, the depth of the transition zone will be altered.

As a result, a mixture of faulted and increasingly metamorphically downgraded rocks, called the *'crush melange'*, will be found on the hanging wall of the fault. Fault gouge and cataclasites gather through cataclastic flow and/or progressive accumulation of cataclastic detritus in an area on the footwall of the fault called the *'crush zone'* [Sibson 1977].

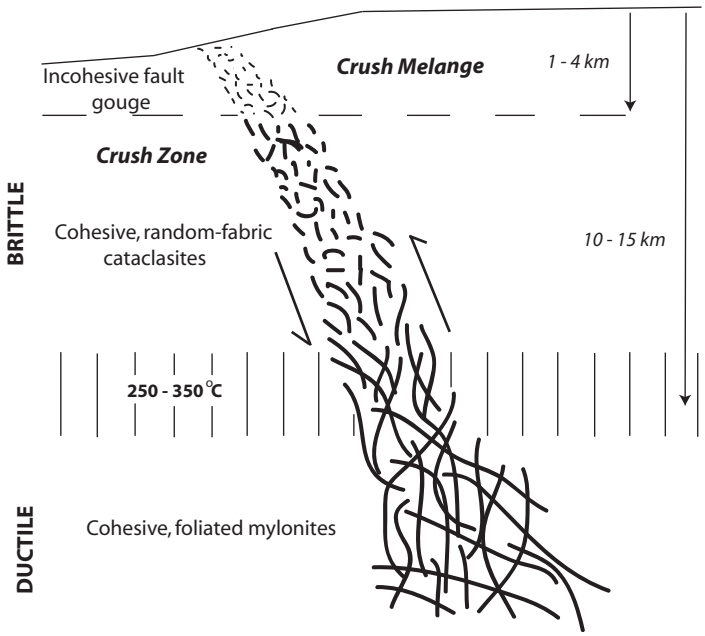

Figure 5.1: Schematic drawing based on the conceptual model for major dip-slip faults proposed by Sibson [1977].

Downgrading of rocks due to faulting

Mechanical processes are the likely causes of seismic velocity reduction in the shallow part of faults [Mooney and Ginzburg 1986, Sibson 1977, Stern and McBride 1998] as high fluid pressure is at greater depths [Smith et al. 1995, Stern et al. 2001]. The amount of velocity variation in the fault-related rocks will depend on which mechanical regimes they have been formed in:

- **Rocks formed in a ductile regime:** The conditions defining the ductile regime are that of high pressure, high temperature and high water content. Thus, these rocks are more likely to be formed as the depth increases. On the fault plane, the ductile and aseismic shearing produces mylonites [Sibson 1977]. There is little or no substantial difference in seismic velocity between the mylonites and their protoliths although their foliation makes them anisotropic [Mooney and Ginzburg 1986].

- **Rocks formed in a brittle regime:** Depending on the depth, cohesive cataclasites or incohesive fault gouge will be produced and stocked on the surface portion of the fault zone [Mooney and Ginzburg 1986, Sibson 1977]. The velocity reductions for cataclasites and fault gouge are suggested to be of the order of 20% and 40 %, respectively [Mooney and Ginzburg 1986].

5.1.2 Model comparison with the findings of this study

LVZ on the southeast of the Alpine fault

The models derived from the refraction first breaks (figures 3.6 – 3.9) show that the seismic velocities on the southeast of the mylonite strip decrease going towards the Alpine fault's surface trace. In this area, seismic velocities of 5 km/s reach 2 km depth. This is coincident with the results of Garrick and Hatherton [1973]'s surface velocity study and this area is satisfactorily explained by the concept of *crush melange* where the increasingly faulted and metamorphically downgraded rocks accumulate [Sibson 1977] on the hanging wall close to the fault's surface trace.

However, we noticed a 5% apparent seismic velocity discrepancy between shots with rays incoming from the northwest (shot points (SP) 14 – 16) and those with rays incoming from the southeast (SP13). This discrepancy could be the consequence of an anisotropic structure in the area, such as that proposed by Little et al. [2002], Sutherland et al. [2006], Wightman and Little [2007], but we rather attribute it to a mixture of anisotropy and three-dimensional multipathing where the rays go through distinct ray paths around the cavities. We also need to bare in mind that the only shot that displays this discrepancy is the one with the smallest charge size and the noisiest shot gather (SP13). Hence, the modelling results (depth estimation, position of the features) might be corrupted due to these imperfections. But as a whole, the four seismic models are reasonably similar to allow us to be confident concerning the velocity structure we propose for the shallow part of the Alpine fault.

A closer insight should be undertaken in the area southeast of the Alpine fault in order to check for evidence and verify whether this velocity discrepancy signifies the presence of an anisotropic structure associated with the Alpine fault.

Basement geometry on the northwest of the Alpine fault

On the northwestern side of the mylonite strip, apart from the concave cavities, the base of the horizons of the Quaternary and Tertiary sediments seem relatively unperturbed. The fact that the Australian plate appears unfaulted contradicts the concept of *crush zone* where cataclastic debris accumulate on the foot wall of the fault [Sibson 1977].

Alpine fault model

The above interpretations enabled us to create a schematic model of the shallow part of the Alpine fault, which can be seen on figure 5.2. On the latter we can see that the formation and accumulation of fault related rocks is predominantly occurring to the southeast of the mylonite strip. The brittle-ductile transition, located at 6 – 8 km depth, marks the upper threshold of mylonite production. The pictured granitic intrusion has no depth or shape constraints but its presence is inferred from the existence of other such features in the area, such as Ralfes knob. To the northwest we can see the kettle holes, which have been carved out in the unperturbed horizons of the Quaternary and Tertiary sediments.

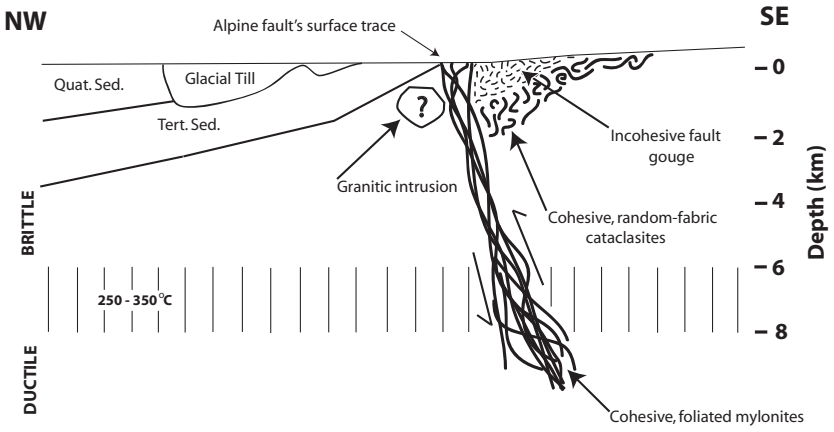

Figure 5.2: Schematic drawing of the model proposed for the shallow part of the Alpine fault.

5.2 Glacial overdeepings and beheaded river mouth

Glacial overdeepings

The geology structure resulting from the seismic models (figures 3.5) show two successive cavities to the northwest of the Alpine fault's surface trace, which are cut into the Quaternary sediments and part of the Tertiary sediments.

From the seismic models (figures 3.6 – 3.9) we can see that the velocity of the material filling the cavities, which is of roughly 2.18 km/s (average between 1.7 and 2.5 km/s), is similar to that of glacial till. Herman and Braun [2007] proposed that during the Otira glaciation, the Whataroa-Perth catchment glacier crossed the Alpine fault's surface trace and entered the Whataroa river flood plain (figure 5.3). We therefore propose those two cavities to be *kettle holes* which mark the path and the terminal extent of a glacier. The cavity that is the closest to the Alpine fault surface trace is about 2 km long and 300 m deep and the furthest one is 4 km long and almost 1 km deep.

This proposition is reinforced by the first gravity model, which showed that the erosional valleys underlying the three main rivers have a characteristic 'U'-shape which is a sign of glacial erosion. The dimensions and position of the cavities are coincident with the negative continuity in the residual gravity field of the flood plain (white outline in figure 4.1). Furthermore, the additional gravity survey in chapter 4 accepted the presence of a body of similar size, shape and material than the kettle holes.

Beheaded river mouth

The glacier's advance proposed by Herman and Braun [2007] indicates that the cavity was carved out by a glacier flowing down the Whataroa River and the strike of their alignment

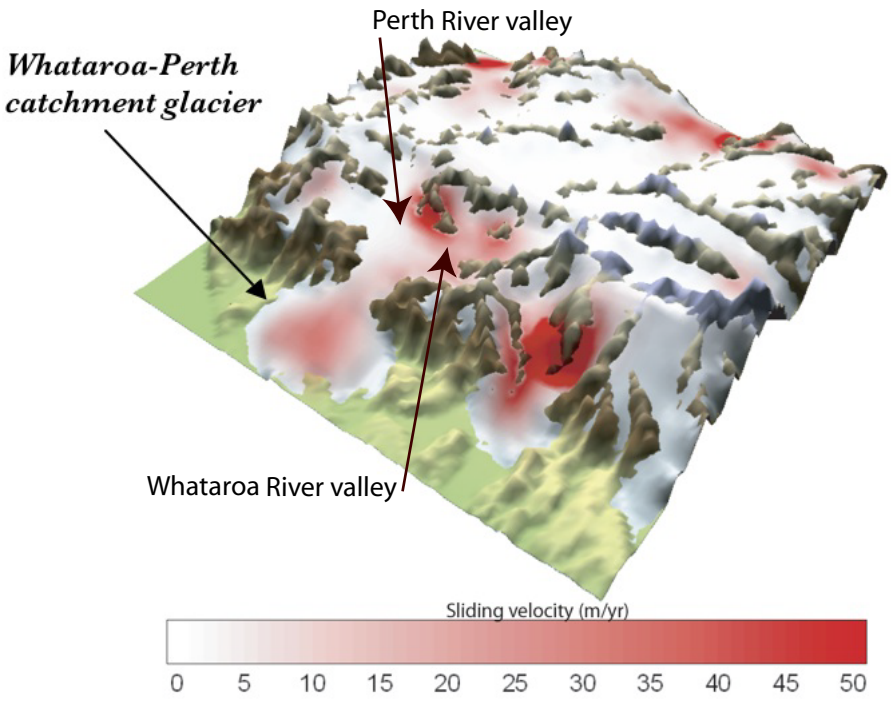

Figure 5.3: This figure shows the suggested advance of the Whataroa-Perth catchment glacier onto the Whataroa River flood plain. *Courtesy of Herman and Braun [2007].*

is sub-parallel to the river valley. We, therefore, propose that the 3.5 km offset between the continuity (marked by the two kettle holes) and the present day Whataroa river mouth (marked by a double black arrow in figure 4.1) is in fact the result of dextral slip along the Alpine fault. This means that the carved kettle holes are in fact the beheaded river mouths of the Whataroa River.

The fact that there are two distinct cavities indicate that the carving must have occurred during two different glacial advances. The literature provides information on the displacement rate along the Alpine fault, based on the offset of glacial landforms detected from aerial photography:

- Estimation of 26 mm/yr over the Late-Quaternary [Sutherland and Norris 1995].
- Mean surface displacement of 23 mm/yr over the interval 79 – 18 Ka [Sutherland et al. 2006].

Considering the latest estimation (23 mm/yr), 3.5 km offset would have taken 150 Ka of dextral slip on the Alpine fault to produce. Studies of atmospheric temperature of the Vostok ice core suggest that the Otira glaciation (100 – 18 Ka) was preceded by a glaciation period of greater extent, which is known as the Waimea glaciation, which culminated at 140 Ka [Petit et al. 1999].

Supposing that the furthest cavity would have then been carved out during the Waimea glaciation, the approximate 3.5 km offset is therefore suggested to have been the result of 140 Ka of dextral strike slip motion. This means that over the last 140 Ka, which is when the glacier ceased prograding, the mean surface displacement along the Alpine fault would be of the order of 25 mm/yr, which is coincident with the estimates of Sutherland and Norris [1995] and Sutherland et al. [2006].

Other such studies could be undertaken in areas similar to the Whataroa River flood plain to measure the offset of glacial erosional valleys and yield a better-constrained displacement rate along the Alpine fault. Flood plain such as the one of the Wanganui River and that of the Waiho River would be appropriate to conduct such studies.

5.3 Summary of the conclusions

The four main conclusions derived from the findings of this thesis are:

1. The Low Velocity Zone on the southeast of the Alpine fault has seismic velocities around 5 km/s reaching a depth of about 2 km.

2. The horizons of the Quaternary and Tertiary sediments, as well as the Australian plate's basement rock appear to be unperturbed.

3. Two kettle holes, which are proposed to have been carved successively during the Waimea and Otira glaciations, are suggested to be the beheaded river mouth of the Whataroa River.

4. We propose a displacement rate for the dextral slip movement on the Alpine fault of 25 mm/yr over the last 140 Ka.

Appendix A

Gravity Meter Calibration Table

NEW TABLE (after calibration)

Counter Units	mGal	Corr. Factor	Counter Units	mGal	Corr. Factor
0	0	1.0541493	3600	3794.405439	1.054899356
100	105.4179302	1.054029291	3700	3899.893374	1.054959361
200	210.8158589	1.053919282	3800	4005.391311	1.055009364
300	316.2137876	1.053709267	3900	4110.889247	1.055039367
400	421.5917148	1.053709267	4000	4216.397184	1.05507937
500	526.9596412	1.053629261	4100	4321.905121	1.055119373
600	632.3275676	1.053579257	4200	4427.413058	1.055149375
700	737.6854933	1.053559255	4300	4532.930995	1.055159376
800	843.043419	1.053569256	4400	4638.448933	1.055199379
900	948.3913439	1.053579257	4500	4743.966871	1.055229381
1000	1053.74927	1.053579257	4600	4849.484809	1.055209379
1100	1159.107195	1.053579257	4700	4955.012747	1.055199379
1200	1264.465121	1.053559255	4800	5060.530685	1.055189378
1300	1369.823047	1.053569256	4900	5166.048623	1.055159376
1400	1475.180972	1.053589258	5000	5271.56656	1.055119373
1500	1580.538898	1.053629261	5100	5377.074497	1.055039367
1600	1685.906824	1.053709267	5200	5482.582434	1.054959361
1700	1791.274751	1.053779272	5300	5588.08037	1.054869354
1800	1896.652678	1.053829276	5400	5693.568306	1.054779347
1900	2002.040606	1.053879279	5500	5799.046241	1.05467934
2000	2107.428534	1.053929283	5600	5904.514175	1.054569331
2100	2212.816462	1.053979287	5700	6009.962107	1.054449322
2200	2318.214391	1.05401929	5800	6115.410039	1.054309312
2300	2423.612319	1.054059293	5900	6220.83797	1.054179302
2400	2529.020249	1.054129298	6000	6326.255901	1.05401929
2500	2634.438179	1.054179302	6100	6431.66383	1.053829276
2600	2739.856109	1.054229306	6200	6537.041757	1.053629261
2700	2845.274039	1.054299311	6300	6642.409684	1.053379242
2800	2950.70197	1.054379317	6400	6747.747608	1.053119222
2900	3056.139902	1.054459323	6500	6853.05553	1.0528192
3000	3161.587834	1.054529328	6600	6958.34345	1.052499176
3100	3267.045768	1.054599334	6700	7063.591368	1.05215915
3200	3372.503701	1.054659338	6800	7168.809283	1.051799123
3300	3477.971635	1.054729343	6900	7273.987195	1.051429095
3400	3583.439569	1.054779347	7000	7379.125104	1.000075232

Table A.1: Calibration table for the Lacoste-Romberg gravitymeter G-179

Appendix B

Terrain Correction Conversion Table

TERRAIN CORRECTION CONVERSION TABLE IN MILLIGALS.
Topography density = 2.67Mg.m^{-3}

Zones	*B*	*C*	*D*	*E*	*F*	*G*
Compartments	2	6	6	8	8	12
Inner Radius	2	16.6	53.3	170.1	390.1	894.9
Outer Radius	16.6	53.3	170.1	390.1	894.9	1529.5

Value (mGals)	***±H (m)***		***±H (m)***		***±H (m)***		***±H (m)***		***±H (m)***		***±H (m)***	
0.01	1	2	4	6	6	11	15	26	22	39	48	83
0.02	2	2	6	8	11	15	26	33	39	50	83	108
0.03	2	3	8	10	15	17	33	39	50	59	108	128
0.04	3	3	10	12	17	20	39	45	59	67	128	145
0.05	3	4	12	13	20	22	45	50	67	74	145	161
0.06	4	4	13	14	22	24	50	54	74	81	161	175
0.07	4	5	14	16	24	26	54	58	81	87	175	188
0.08	5	6	16	17	26	28	58	62	87	93	188	201
0.09	6	6	17	18	28	30	62	66	93	98	201	212
0.1	6	7	18	20	30	31	66	70	98	103	212	224
0.11	7	7	20	21	31	33	70	73	103	108	224	234
0.12	7	8	21	22	33	34	73	76	108	113	234	245
0.13	8	9	22	24	34	36	76	80	113	118	245	255
0.14	9	9	24	25	36	38	80	83	118	122	255	264
0.15	9	10	25	26	38	39	83	86	122	126	264	274
0.16	10	11	26	28	39	40	86	89	126	131	274	283
0.17	11	12	28	29	40	42	89	92	131	135	283	292
0.18	12	13	29	30	42	43	92	95	135	139	292	300
0.19	13	14	30	32	43	45	95	97	139	143	300	309
0.2	14	15	32	33	45	46	97	100	143	146	309	317
0.21	15	16	33	35	46	47	100	103	146	150	317	325
0.22	16	17	35	36	47	49	103	106	150	154	325	333
0.23	17	19	36	38	49	50	106	108	154	157	333	341
0.24	19	20	38	39	50	51	108	111	157	161	341	349
0.25	20	22	39	41	51	53	111	114	161	164	349	356
0.26	22	24	41	43	53	54	114	116	164	168	356	364
0.27	24	26	43	45	54	55	116	119	168	171	364	371
0.28	26	28	45	46	55	57	119	121	171	174	371	378
0.29	28	31	46	48	57	58	121	124	174	178	378	385
0.3	31	35	48	50	58	59	124	126	178	181	385	392

Based on the work of Hammer (1939).

Table B.1: Conversion table for the terrain corrections

Appendix C

Reduction of Gravity Data

	COORDINATES				ELEVATION	TIME	GRAVITY			
	Northings (S)		Eastings (E)		Corr. height	Mean time	Rdg's Mean	Conversion	Converted	Drift Corr.
Location	Lat	NZMG	Long.	NZMG	m	dec. hours			mGals	mGals
N1	43.2836	5765828	170.3226	2292749	79.46	12.76	3871.95	75.91	4081.30	4081.29
N2	43.2829	5765865	170.3078	2291538	67.98	16.35	3877.17	81.42	4086.81	4086.81
N3	43.2715	5767130	170.3016	2291007	56.46	19.00	3878.31	82.62	4088.01	4088.04
N5	43.2659	5767764	170.3117	2291802	50.23	17.21	3877.62	81.89	4087.28	4087.29
N7	43.2619	5768242	170.3215	2292576	46.12	17.55	3876.74	80.96	4086.35	4086.37
N9	43.2573	5768777	170.3319	2293409	42.87	17.85	3875.56	79.72	4085.11	4085.12
N11	43.2583	5768689	170.3432	2294335	41.49	18.27	3875.78	79.95	4085.34	4085.36
N13	43.2575	5768834	170.3606	2294733	44.42	13.32	3873.96	78.03	4083.42	4083.40
N14	43.2505	5769621	170.3634	2295937	41.70	10.02	3876.02	80.20	4085.59	4085.58
B	43.2467	5770238	170.3680	2296332	44.20	18.59	3875.65	79.81	4085.20	4085.22
N17	43.2473	5770008	170.3803	2297287	44.07	9.71	3871.28	75.20	4080.59	4080.60
N19	43.2431	5770526	170.3956	2298531	43.73	13.85	3866.85	70.52	4075.91	4075.90
N21	43.2395	5770930	170.4033	2299166	41.25	14.52	3864.77	68.34	4073.73	4073.71
N22	43.2371	5771211	170.4105	2299721	39.98	16.10	3864.61	68.16	4073.55	4073.52
N23	43.2367	5771271	170.4156	2300135	38.50	15.22	3865.29	68.88	4074.27	4074.24
N24	43.2359	5771374	170.4189	2300403	38.56	15.62	3865.24	68.83	4074.22	4074.19
N25	43.2315	5771884	170.4261	2300965	36.58	11.33	3866.84	70.52	4075.91	4075.88
N26	43.2302	5772030	170.4309	2301343	45.82	11.61	3864.13	67.66	4073.05	4073.02
N27	43.2284	5772249	170.4370	2301829	60.78	10.41	3860.43	63.75	4069.14	4069.13
N28	43.2322	5771840	170.4438	2302408	76.59	10.89	3856.27	59.36	4064.75	4064.73
N29	43.2348	5771577	170.4498	2302892	94.56	10.65	3852.47	55.36	4060.75	4060.73
N30	43.2404	5770965	170.4588	2303645	132.41	18.68	3843.32	45.70	4051.09	4051.04
A		5765865		2295182		12.27	3874.32	78.41	4083.80	4083.79
BS	43.2942	5764883	170.4118	2300026	80.77	17.37	3851.57	54.40	4059.79	4059.76

Table C.1: Reduction of the gravity data

	CALCULATIONS OF BOUGUER ANOMALY							
Location	**gobs**	**g(lat)**	**Dg(fh)**	**Inner Zone**	**Outer Zone**	**TC Sum**	**gpredicted**	**Bouguer A.**
	mGals	*mGals*	*mGals*	*mGals*	*mGals*	*mGals*	*mGals*	*mGals*
N1	980430.25	980474.56	-15.63	0.3	5.00	5.30	980453.63	-23.37
N2	980435.78	980474.49	-13.37	0.15	3.35	3.50	980457.62	-21.84
N3	980437.00	980473.47	-11.11	0.22	2.40	2.62	980459.74	-22.74
N5	980436.25	980472.96	-9.88	0	2.19	2.19	980460.90	-24.64
N7	980435.33	980472.60	-9.07	0	2.17	2.17	980461.35	-26.02
N9	980434.09	980472.18	-8.43	0	2.15	2.15	980461.60	-27.51
N11	980434.32	980472.28	-8.16	0	2.39	2.39	980461.72	-27.40
N13	980432.37	980472.20	-8.74	0	2.42	2.42	980461.04	-28.68
N14	980434.55	980471.57	-8.20	0	2.34	2.34	980461.03	-26.48
B	980434.18	980471.23	-8.69	0	2.19	2.19	980460.35	-26.16
N17	980429.56	980471.29	-8.67	0	2.59	2.59	980460.03	-30.47
N19	980424.86	980470.90	-8.60	0	2.89	2.89	980459.41	-34.55
N21	980422.67	980470.58	-8.11	0	3.05	3.05	980459.41	-36.74
N22	980422.48	980470.36	-7.86	0	3.27	3.27	980459.23	-36.74
N23	980423.21	980470.33	-7.57	0	3.57	3.57	980459.19	-35.98
N24	980423.15	980470.26	-7.58	0	3.74	3.74	980458.93	-35.78
N25	980424.84	980469.86	-7.20	0.09	3.79	3.88	980458.79	-33.95
N26	980421.99	980469.74	-9.01	0.16	3.99	4.15	980456.58	-34.60
N27	980418.09	980469.58	-11.96	0.04	4.24	4.28	980453.34	-35.25
N28	980413.70	980469.92	-15.07	0.02	5.46	5.48	980449.37	-35.68
N29	980409.69	980470.16	-18.60	0	6.91	6.91	980444.65	-34.96
N30	980400.01	980470.67	-26.05	0	11.89	11.89	980432.73	-32.72
A	980432.76							
BS	980408.72	980475.51	-15.89			14.10	980445.52	-36.80

Table C.2: Reduction of the gravity data (continued)

Appendix D

Regional Gradient Reduction

	Northings	Eastings	x'	y'	Rx	BA	BA-N30	regional corr	Residual
Station	NZMG	NZMG	m	m	m	mGals	mGals	mGals	mGals
11	5773740	2302650	-995	2775	2587	-29.60	3.13	-1.59	1.53
12	5769250	2285300	-18345	-1715	12572	-27.24	5.49	-7.74	-2.26
88	5772440	2296810	-6835	1475	6088	-35.54	-2.82	-3.75	-6.57
89	5771200	2296560	-7085	235	5452	-30.41	2.31	-3.36	-1.05
90	5770000	2296020	-7625	-965	5058	-26.15	6.58	-3.12	3.46
91	5768850	2296580	-7065	-2115	3875	-27.37	5.35	-2.39	2.96
92	5768090	2296840	-6805	-2875	3176	-29.39	3.33	-1.96	1.38
93	5767420	2297310	-6335	-3545	2380	-30.42	2.30	-1.47	0.84
94	5767140	2297450	-6195	-3825	2089	-30.68	2.05	-1.29	0.76
95	5766550	2297590	-6055	-4415	1592	-30.91	1.82	-0.98	0.83
96	5766170	2297480	-6165	-4795	1422	-30.82	1.90	-0.88	1.03
97	5766050	2297930	-5715	-4915	1006	-31.11	1.61	-0.62	0.99
233	5768730	2288960	-14685	-2235	9491	-20.48	12.24	-5.85	6.40
234	5766000	2292670	-10975	-4965	4904	-19.40	13.32	-3.02	10.30
A=235	5766780	2295170	-8475	-4185	3554	-24.86	7.87	-2.19	5.68
236	5770780	2293960	-9685	-185	7116	-25.29	7.43	-4.38	3.05
237	5770230	2296340	-7305	-735	4972	-26.11	6.62	-3.06	3.55
238	5772440	2296850	-6795	1475	6059	-35.05	-2.32	-3.73	-6.06
239	5775360	2296750	-6895	4395	8073	-36.31	-3.59	-4.97	-8.56
240	5779610	2296490	-7155	8645	11091	-34.11	-1.39	-6.83	-8.22
243	5769670	2301150	-2495	-1295	1004	-32.29	0.43	-0.62	-0.19
244	5778310	2303380	-265	7345	5078	-30.22	2.50	-3.13	-0.62
337	5774990	2299230	-4415	4025	5974	-25.54	7.18	-3.68	3.50
501	5784730	2286890	-16755	13765	21668	-22.44	10.28	-13.35	-3.06
502	5780980	2291620	-12025	10015	15641	-32.59	0.13	-9.63	-9.50
N1	5765828	2292749	-10896	-5137	4731	-23.37	9.35	-2.91	6.44
N2	5765865	2291538	-12107	-5100	5661	-21.84	10.88	-3.49	7.39
N3	5767130	2291007	-12638	-3835	6898	-22.74	9.98	-4.25	5.73
N5	5767764	2291802	-11843	-3201	6725	-24.64	8.08	-4.14	3.93
N7	5768242	2292576	-11069	-2723	6464	-26.02	6.70	-3.98	2.72
N9	5768777	2293409	-10236	-2188	6197	-27.51	5.21	-3.82	1.39
N11	5768689	2294335	-9310	-2276	5446	-27.40	5.32	-3.35	1.97
N13	5768834	2294733	-8912	-2131	5245	-28.68	4.05	-3.23	0.81
N14	5769621	2295937	-7708	-1344	4868	-26.48	6.24	-3.00	3.24
B	5770238	2296332	-7313	-727	4983	-26.16	6.56	-3.07	3.49
N17	5770008	2297287	-6358	-957	4116	-30.47	2.25	-2.54	-0.28
N19	5770526	2298531	-5114	-439	3531	-34.55	-1.83	-2.17	-4.00
N21	5770930	2299166	-4479	-35	3324	-36.74	-4.02	-2.05	-6.07
N22	5771211	2299721	-3924	246	3096	-36.74	-4.02	-1.91	-5.93
N23	5771271	2300135	-3510	306	2827	-35.98	-3.26	-1.74	-5.00
N24	5771374	2300403	-3242	409	2695	-35.78	-3.06	-1.66	-4.72
N25	5771884	2300965	-2680	919	2614	-33.95	-1.22	-1.61	-2.83
N26	5772030	2301343	-2302	1065	2428	-34.60	-1.88	-1.50	-3.37
N27	5772249	2301829	-1816	1284	2210	-35.25	-2.53	-1.36	-3.89
N28	5771840	2302408	-1237	875	1506	-35.68	-2.96	-0.93	-3.88
N29	5771577	2302892	-753	612	969	-34.96	-2.24	-0.60	-2.83
N30	5770965	2303645	0	0	0	-32.72	0.00	0.00	0.00

Reference line angle	in radians	0.7266
	in degrees	41.634
Refrence Point	Easting	2303645
	Northing	5770965
Reg. gdt	mGals/km	1.2685

Table D.1: Determination of the regional gradient

Appendix E

First Break Pick Files and Shot Gathers

0	6	0	1	
1252	-0.04	0.0073	0	1
1256	0.216	0.0329	0	1
1260	0.655	0.1828	0	1
1264	0.85	0.2148	0	1
1272	1.549	0.399	0	1
1276	1.987	0.3171	0	1
1280	2.36	0.2863	0	1
1288	3.39	0.2932	0	1
1292	3.629	0.3147	0	1
1296	4.08	0.5344	0	1
1300	4.271	0.475	0	1
1304	4.675	0.4615	0	1
1308	5.063	0.3964	0	1
1312	5.509	0.5423	0	1
1316	5.953	0.4575	0	1
1320	6.537	0.4903	0	1
1324	6.909	0.4999	0	1
1328	7.156	0.5031	0	1
1332	7.596	0.5464	0	1
1336	8.051	0.5081	0	1
1348	9.37	0.5441	0	1
1356	10.215	0.5678	0	1
1360	10.793	0.6398	0	1
1364	11.112	0.5432	0	1
1368	11.57	0.6489	0	1
1372	12.003	0.6297	0	1
1376	12.442	0.6246	0	1
1380	12.884	0.6834	0	1
1384	13.342	0.7065	0	1
1392	14.191	0.8576	0	1
1396	14.603	0.9546	0	1
1400	14.99	0.9038	0	1
1408	15.831	0.9432	0	1
1412	16.137	0.9732	0	1
1420	17.096	1.0719	0	1
1424	17.567	1.0589	0	1
1428	17.979	1.0545	0	1
1436	18.557	1.2876	0	1
1440	19.486	1.3409	0	1
1444	19.866	1.324	0	1
1448	20.226	1.3529	0	1
1452	20.643	1.4609	0	1
1456	21.069	1.3957	0	1
1460	21.342	1.3997	0	1

Table E.1: Pick file for Shot Point 13

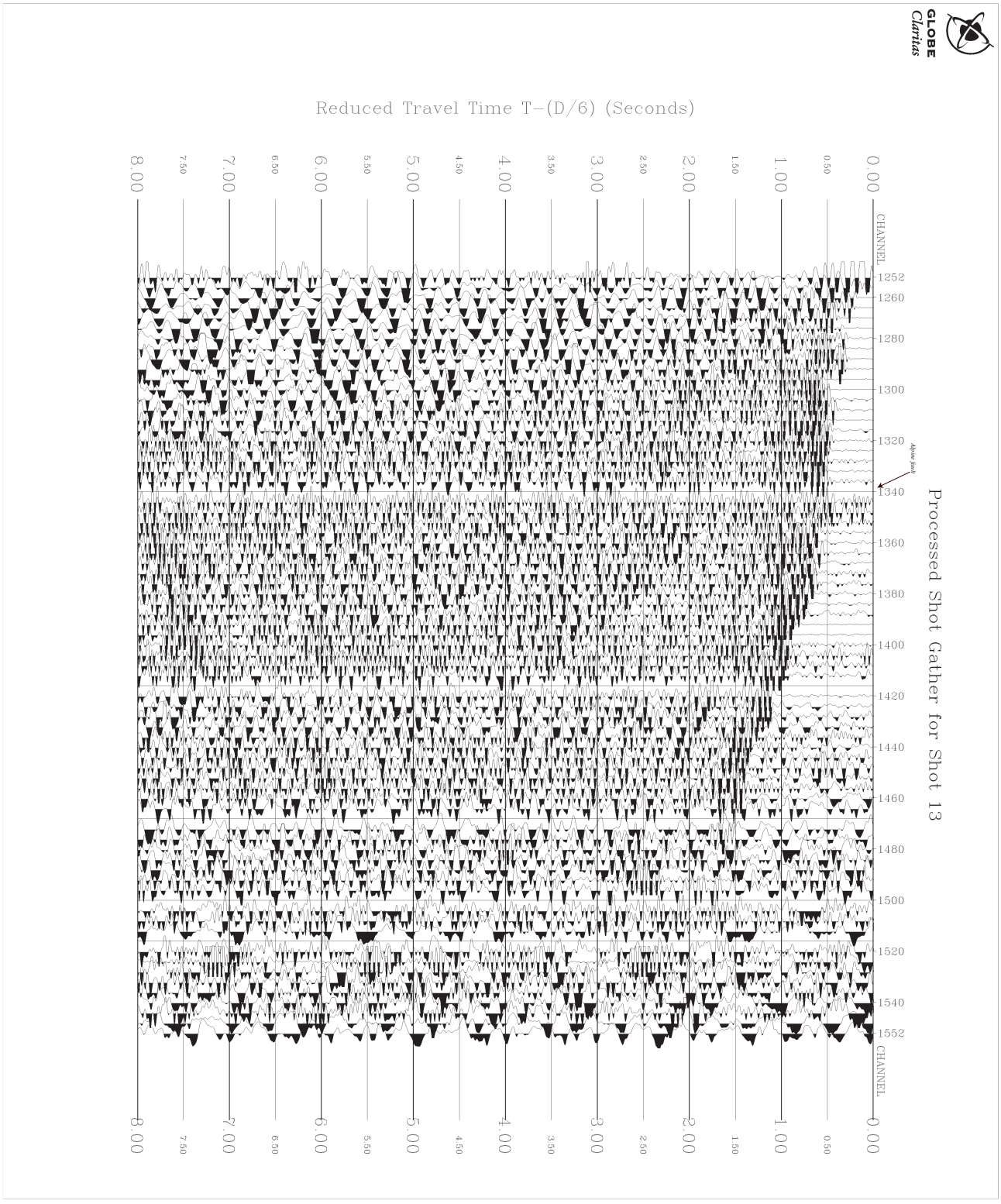

Figure E.1: Processed shot gather of Shot Point 13

12.36	6	0	1	
1252	-12.399	0.4882	0	1
1256	-12.144	0.44	0	1
1260	-11.705	0.5703	0	1
1264	-11.509	0.5778	0	1
1272	-10.811	0.5118	0	1
1276	-10.373	0.5055	0	1
1280	-10	0.4713	0	1
1288	-8.969	0.4841	0	1
1292	-8.73	0.4352	0	1
1296	-8.279	0.4617	0	1
1300	-8.088	0.4742	0	1
1304	-7.685	0.5052	0	1
1308	-7.297	0.4125	0	1
1312	-6.85	0.4484	0	1
1316	-6.406	0.3628	0	1
1320	-5.823	0.4325	0	1
1324	-5.451	0.4134	0	1
1328	-5.204	0.4532	0	1
1332	-4.764	0.4556	0	1
1336	-4.308	0.3621	0	1
1344	-3.426	0.2711	0	1
1348	-2.99	0.3277	0	1
1352	-2.553	0.3555	0	1
1356	-2.144	0.2694	0	1
1360	-1.567	0.217	0	1
1364	-1.247	0.2979	0	1
1368	-0.79	0.1988	0	1
1372	-0.356	0.0404	0	1
1376	0.082	0	0	1
1380	0.525	0.0794	0	1
1384	0.983	0.2141	0	1
1388	1.301	0.3674	0	1
1392	1.831	0.4199	0	1
1396	2.243	0.4893	0	1
1400	2.63	0.4585	0	1
1404	3.047	0.4753	0	1
1408	3.471	0.4951	0	1
1412	3.777	0.5317	0	1
1420	4.737	0.7291	0	1
1424	5.207	0.7484	0	1
1428	5.619	0.7959	0	1
1432	6.197	0.9753	0	1
1436	6.57	1.009	0	1
1440	7.126	1.048	0	1
1444	7.507	1.1119	0	1
1448	7.866	1.1794	0	1
1452	8.284	1.3107	0	1
1456	8.709	1.2844	0	1
1460	8.983	1.2492	0	1
1464	9.403	1.2474	0	1
1472	10.147	1.371	0	1
1476	10.54	1.3847	0	1
1480	10.921	1.4535	0	1
1484	11.322	1.4599	0	1
1488	11.614	1.486	0	1
1492	12.098	1.5249	0	1
1496	12.524	1.5379	0	1
1504	13.333	1.5111	0	1
1508	13.668	1.555	0	1
1512	13.955	1.616	0	1
1520	14.815	1.6602	0	1
1524	15.242	1.6576	0	1
1528	15.468	1.6766	0	1
1532	15.701	1.7338	0	1
1536	16.136	1.7178	0	1
1540	16.441	1.7546	0	1
1544	16.709	1.7751	0	1

Table E.2: Pick file for Shot Point 14

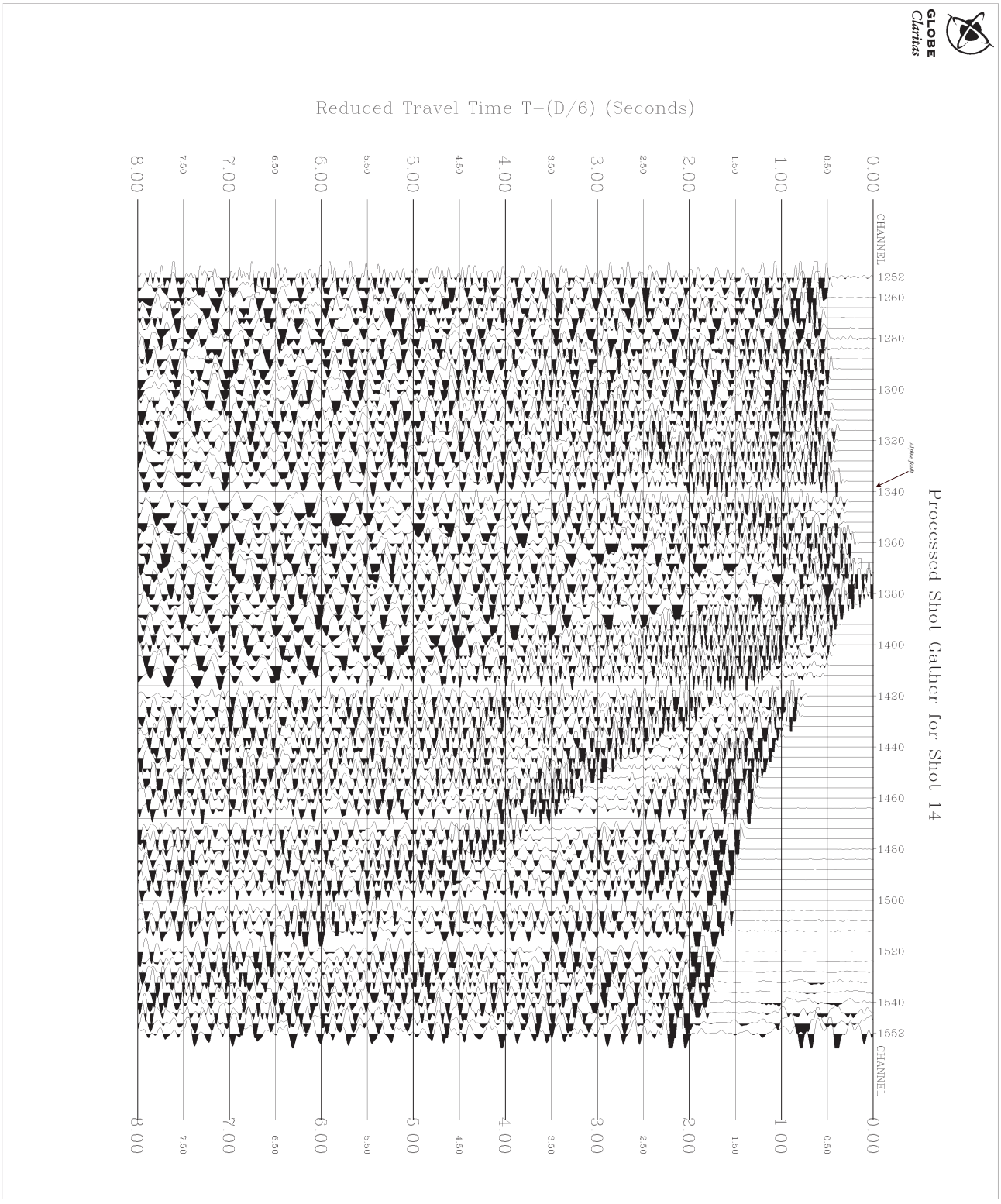

Figure E.2: Processed shot gather of Shot Point 14

23.08	6	0	1	
1252	-23.071	1.2903	0	1
1256	-22.816	1.2526	0	1
1260	-22.377	1.3845	0	1
1264	-22.181	1.3897	0	1
1272	-21.483	1.3506	0	1
1276	-21.045	1.3445	0	1
1280	-20.672	1.3223	0	1
1284	-20.179	1.3822	0	1
1288	-19.641	1.3463	0	1
1292	-19.402	1.311	0	1
1296	-18.951	1.3365	0	1
1300	-18.76	1.3859	0	1
1304	-18.357	1.4142	0	1
1308	-17.968	1.3525	0	1
1312	-17.522	1.3798	0	1
1316	-17.078	1.3223	0	1
1320	-16.495	1.3779	0	1
1324	-16.123	1.4439	0	1
1328	-15.875	1.4956	0	1
1332	-15.436	1.5282	0	1
1336	-14.98	1.4222	0	1
1344	-14.098	1.4077	0	1
1348	-13.661	1.4536	0	1
1352	-13.224	1.5181	0	1
1356	-12.816	1.4101	0	1
1360	-12.239	1.3996	0	1
1364	-11.919	1.4847	0	1
1368	-11.462	1.4411	0	1
1372	-11.028	1.423	0	1
1376	-10.59	1.4242	0	1
1380	-10.147	1.4657	0	1
1384	-9.689	1.4951	0	1
1388	-9.371	1.513	0	1
1392	-8.841	1.531	0	1
1396	-8.429	1.5531	0	1
1400	-8.042	1.5001	0	1
1404	-7.625	1.4403	0	1
1408	-7.201	1.3905	0	1
1412	-6.895	1.3619	0	1
1420	-5.935	1.3628	0	1
1424	-5.465	1.3205	0	1
1428	-5.053	1.3053	0	1
1432	-4.475	1.2631	0	1
1436	-4.101	1.1354	0	1
1440	-3.546	1.0121	0	1
1444	-3.165	0.9466	0	1
1448	-2.806	0.8135	0	1
1452	-2.388	0.8068	0	1
1456	-1.963	0.6773	0	1
1460	-1.689	0.6092	0	1
1464	-1.269	0.3729	0	1
1472	-0.525	0.1536	0	1
1476	-0.132	0	0	1
1480	0.249	0.133	0	1
1484	0.65	0.3382	0	1
1488	0.943	0.4529	0	1
1492	1.427	0.6604	0	1
1496	1.853	0.735	0	1
1504	2.661	0.8877	0	1
1508	2.997	0.9547	0	1
1512	3.283	1.0343	0	1
1520	4.143	1.1786	0	1
1524	4.57	1.2124	0	1
1528	4.796	1.2886	0	1
1532	5.029	1.5595	0	1
1536	5.464	1.548	0	1
1540	5.769	1.6246	0	1
1544	6.037	1.6907	0	1
1548	6.294	1.7218	0	1
1552	6.669	1.7829	0	1

Table E.3: Pick file for Shot Point 15

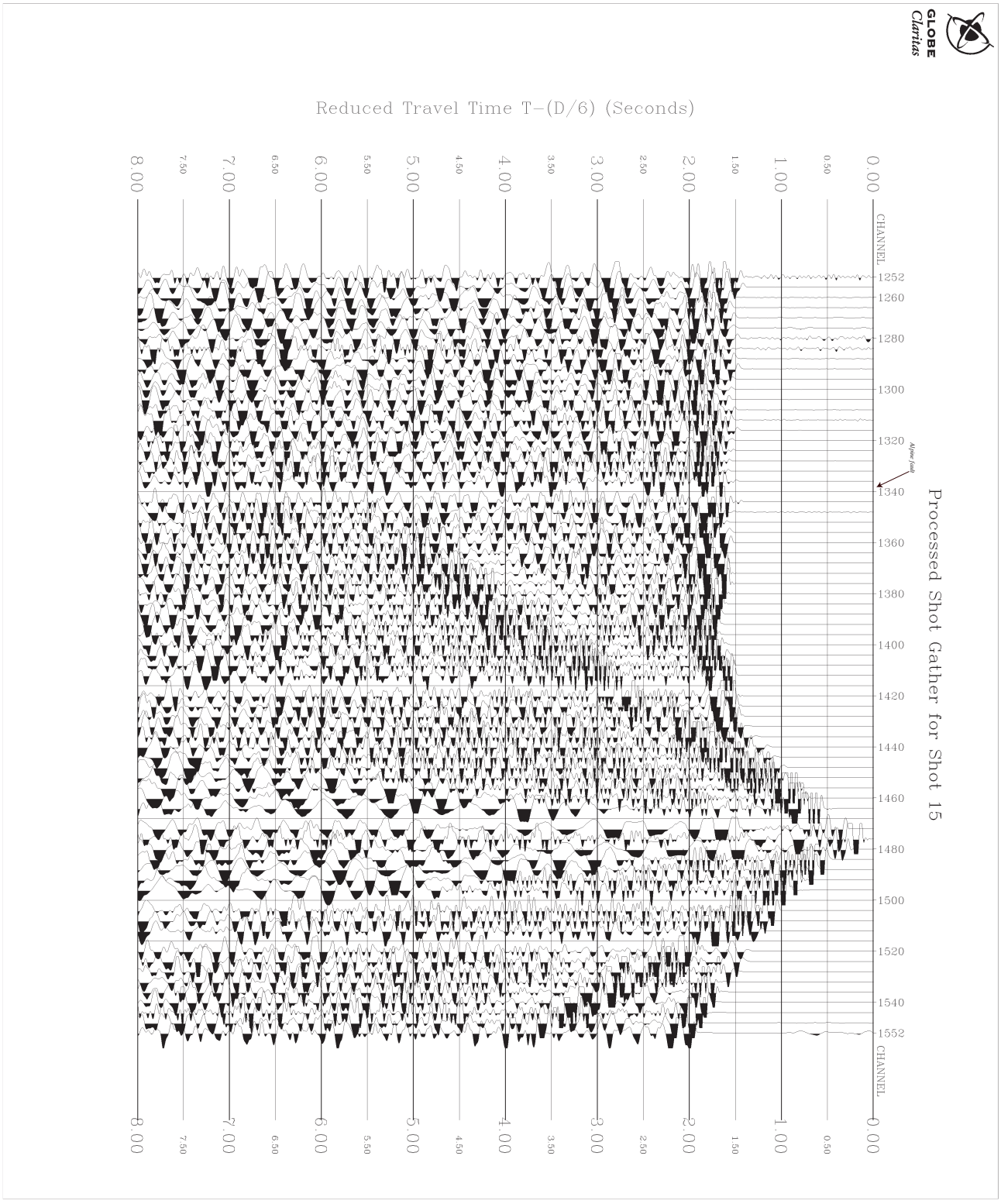

Figure E.3: Processed shot gather of Shot Point 15

26.32	6	0	1	
1252	-26.367	1.4595	0	1
1256	-26.111	1.3895	0	1
1260	-25.672	1.5375	0	1
1264	-25.477	1.5592	0	1
1272	-24.778	1.5138	0	1
1276	-24.34	1.5256	0	1
1280	-23.967	1.5019	0	1
1288	-22.937	1.5223	0	1
1292	-22.698	1.4756	0	1
1296	-22.247	1.5363	0	1
1300	-22.056	1.5536	0	1
1304	-21.652	1.5549	0	1
1308	-21.264	1.588	0	1
1312	-20.818	1.6248	0	1
1316	-20.374	1.5677	0	1
1320	-19.79	1.6251	0	1
1324	-19.418	1.5952	0	1
1328	-19.171	1.6251	0	1
1332	-18.731	1.6496	0	1
1336	-18.276	1.5615	0	1
1344	-17.393	1.5164	0	1
1348	-16.957	1.6303	0	1
1352	-16.52	1.6029	0	1
1356	-16.112	1.5621	0	1
1360	-15.534	1.5742	0	1
1364	-15.215	1.6524	0	1
1368	-14.757	1.6159	0	1
1372	-14.324	1.5999	0	1
1376	-13.885	1.6181	0	1
1380	-13.443	1.6551	0	1
1384	-12.985	1.6929	0	1
1388	-12.667	1.7246	0	1
1392	-12.136	1.7535	0	1
1396	-11.724	1.7827	0	1
1400	-11.337	1.721	0	1
1404	-10.921	1.6925	0	1
1408	-10.496	1.6255	0	1
1412	-10.19	1.6168	0	1
1420	-9.231	1.6275	0	1
1424	-8.76	1.6637	0	1
1428	-8.348	1.6567	0	1
1432	-7.77	1.6544	0	1
1436	-7.397	1.6403	0	1
1440	-6.841	1.5912	0	1
1444	-6.461	1.5712	0	1
1448	-6.101	1.5329	0	1
1452	-5.684	1.5379	0	1
1456	-5.258	1.4055	0	1
1460	-4.985	1.3589	0	1
1464	-4.564	1.274	0	1
1472	-3.82	1.1559	0	1
1476	-3.427	1.0695	0	1
1480	-3.047	1.0426	0	1
1484	-2.646	0.9667	0	1
1488	-2.353	0.9084	0	1
1492	-1.869	0.7823	0	1
1496	-1.443	0.6095	0	1
1504	-0.635	0.1838	0	1
1508	-0.299	0.1016	0	1
1512	-0.013	0	0	1
1520	0.847	0.3518	0	1
1524	1.274	0.5365	0	1
1528	1.501	0.6999	0	1
1532	1.734	0.965	0	1
1536	2.169	0.971	0	1
1540	2.474	1.137	0	1
1544	2.741	1.285	0	1
1548	2.998	1.397	0	1
1552	3.374	1.4927	0	1

Table E.4: Pick file for Shot Point 16

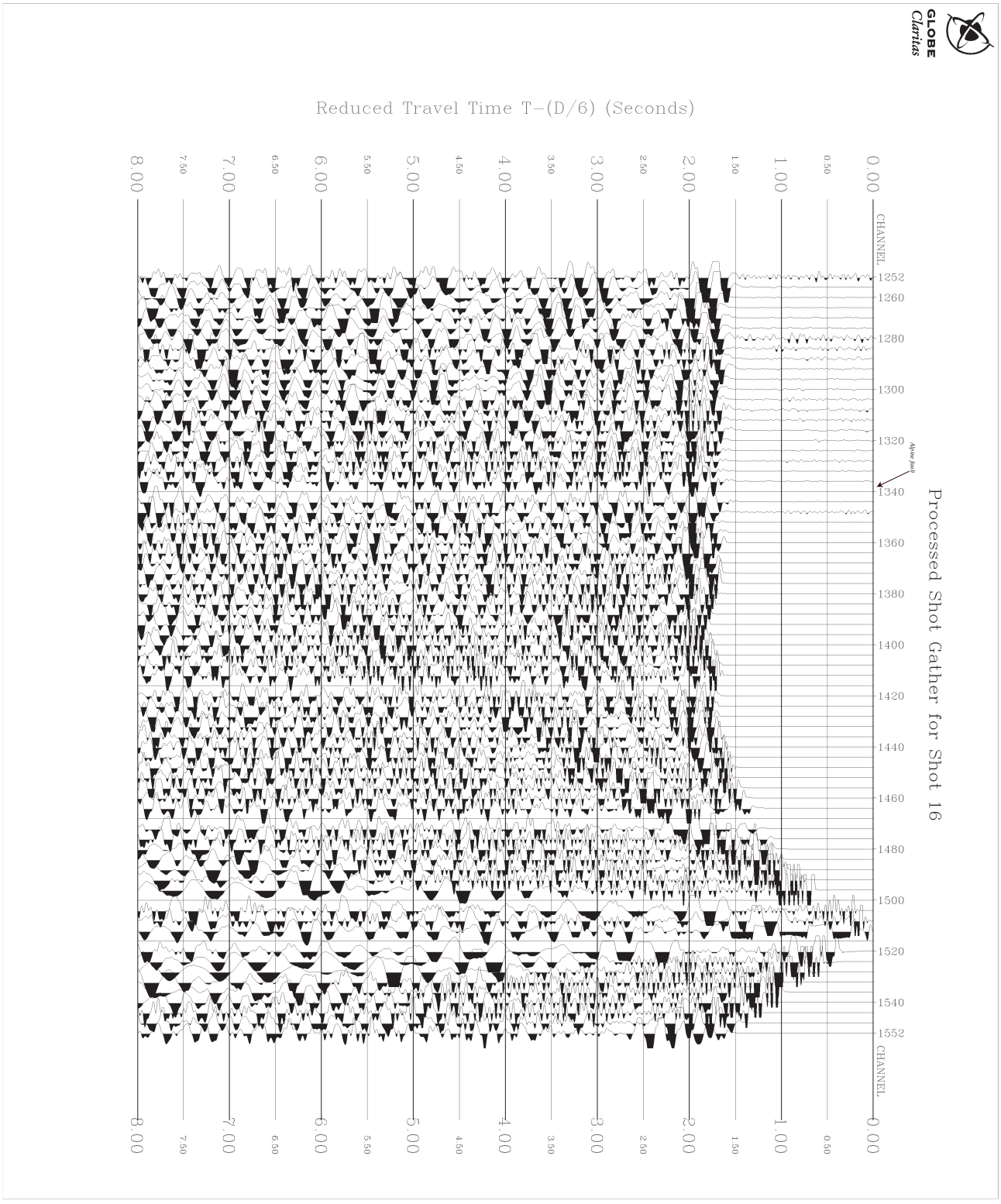

Figure E.4: Processed shot gather of Shot Point 16

Appendix F

GNS Data

SHEET	STATNUM	X_COORD	Y_COORD	HEIGHT	HCODE	OBSGRAV	METERNO	YEAR	MONTH	DAY	ICORR	OCORR	ITOPC	TOPC	FAA	BA	ISO
17	11	5773740	2302650	44.20	2	54194.60	96	53	0	0	0.30	54.10	4	-39.30	-354.50	-310.00	31.40
17	12	5769250	2285300	27.20	2	54344.90	96	53	0	0	0.50	10.00	4	-27.80	-288.60	-280.60	-38.80
17	88	5772440	2296810	29.60	2	54259.30	283	64	0	0	0.00	17.40	4	-37.10	-344.00	-322.40	-15.50
17	89	5771200	2296560	35.70	2	54305.30	283	64	0	0	0.00	20.70	4	-38.70	-289.20	-269.40	49.50
17	90	5770000	2296020	38.20	2	54347.80	283	64	0	0	0.00	25.50	4	-32.90	-248.60	-232.60	97.40
17	91	5768850	2296580	48.20	2	54320.60	283	64	0	0	0.00	30.20	4	-35.00	-254.30	-242.70	104.10
17	92	5768090	2296840	52.10	2	54293.70	283	64	0	0	0.00	35.50	4	-36.30	-275.40	-261.50	96.50
17	93	5767420	2297310	55.50	2	54270.30	283	64	0	0	0.00	47.50	4	-37.50	-293.90	-270.50	99.00
17	94	5767140	2297450	59.00	2	54257.10	283	64	0	0	0.00	53.50	4	-38.10	-298.60	-272.50	101.20
17	95	5766550	2297590	63.10	2	54238.10	283	64	0	0	0.00	67.00	4	-38.90	-309.80	-273.90	107.60
17	96	5766170	2297480	64.60	2	54232.10	283	64	0	0	0.00	74.00	4	-39.30	-314.20	-272.60	112.40
17	97	5766050	2297930	65.20	2	54226.80	283	64	0	0	0.30	76.00	4	-40.00	-318.70	-274.80	115.10
17	98	5765750	2299030	75.00	2	54160.90	283	64	0	0	13.80	80.00	4	-35.80	-357.10	-310.70	93.80
17	99	5765210	2299510	78.20	2	54129.00	283	64	0	0	18.30	87.80	4	-36.70	-383.60	-327.60	87.00
17	100	5764350	2300290	87.20	2	54065.00	283	64	0	0	1.30	108.10	4	-38.20	-426.90	-376.10	54.60
17	101	5764130	2300290	85.20	2	54067.80	283	64	0	0	0.30	112.50	4	-38.50	-432.20	-375.40	58.00
17	102	5763770	2300390	86.10	2	54060.90	283	64	0	0	0.90	118.50	4	-39.00	-439.30	-376.40	61.80
17	103	5763200	2300480	88.70	2	54039.00	283	64	0	0	3.30	127.20	4	-35.20	-457.70	-390.50	56.50
17	104	5762620	2300720	92.70	2	54019.60	283	64	0	0	1.00	136.20	4	-35.80	-469.50	-399.30	56.10
17	105	5761850	2300990	100.60	2	53969.30	283	64	0	0	2.90	148.30	4	-36.60	-501.70	-425.50	40.40
17	233	5768730	2288960	57.70	2	54383.10	96	62	7	3	0.00	17.00	16	-31.60	-161.50	-177.10	106.00
17	234	5766000	2292670	82.20	2	54344.60	96	62	7	3	0.00	41.10	16	-32.80	-147.50	-164.80	183.00
17	235	5766780	2295170	54.70	2	54324.30	96	62	7	3	0.00	55.30	16	-36.10	-247.00	-216.30	141.80
17	236	5770780	2293960	44.20	2	54341.50	96	62	7	4	0.00	21.70	16	-37.10	-229.40	-219.70	81.20
17	237	5770230	2296340	44.20	2	54338.00	96	62	7	4	0.00	22.10	16	-36.30	-238.00	-228.80	101.40
17	238	5772440	2296850	33.50	2	54257.50	96	62	7	4	0.00	16.50	16	-37.00	-333.80	-317.50	-10.20
17	239	5775360	2296750	30.50	2	54233.70	96	62	7	4	0.00	9.90	16	-32.70	-343.10	-334.40	-59.80
17	240	5779610	2296490	30.50	2	54223.40	96	62	7	4	0.00	7.70	16	-29.70	-319.00	-315.50	-88.50
17	243	5769670	2301150	77.70	2	54162.50	96	62	7	4	0.00	75.60	16	-42.00	-315.90	-284.50	91.20
17	244	5778310	2303380	77.70	2	54121.80	96	62	7	4	20.50	47.10	16	-32.60	-287.10	-273.10	23.70
17	337	5774990	2299230	6.10	2	54234.30	106	69	5	24	0.00	17.10	17	-35.90	-421.40	-375.30	-76.70
17	501	5784730	2286890	1.80	1	54358.40	106	75	11	12	1.50	0.30	18	-20.70	-228.40	-208.00	-104.70
17	502	5780980	2291620	11.00	2	54270.00	106	75	11	12	0.30	2.00	18	-25.30	-320.10	-304.80	-130.00

Table F.1: The GNS data used for modeling

References

Avendonk, H. J. v., Holbrook, S., Okaya, D., Austin, J., Davey, F., and Stern, T. (2004). Continental crust under compression: a seismic refraction study of south island geophysical transect i, south island, new zealand. *J. Geophys. Res.*, 109:B06302.

Beaumont, C., Kamp, P. J., Hamilton, J., and Fullsack, P. (1996). The continental collision zone, south island, new zealand: Comparison of geodynamical and observations. *J. Geophys. Res.*, 10(B2):3333–3359.

Beavan, J., Moore, M., Pearson, C., Henderson, M., Parsons, B., Bourne, S., England, P., Walcott, R., Blick, G., Darby, D., and Hodgkinson, K. (1999). Crustal deformation during 1994-1998 due to oblique continental collision in the central southern alps, new zealand, and implications for seismic potential of the alpine fault. *J. Geophys. Res.*, 104(B11):25233–25255.

Blythe, A. (1998). Active tectonics and ultrahigh-pressure rocks. In Liou, B. H. and J.G., editors, *When continents collide: Geodynamics and Geochemistry of Ultrahigh-pressure rocks*, pages 141–160. Kluwer Academic Publishers.

Braun, J. and Beaumont, C. (1995). Three-dimensional numerical experiments of strain partitionning at oblique plate boundaries: Implications for contrasting tectonic styles in the southern coast ranges, california, and central south island, new zealand. *J. Geophys. Res.*, 100(B9):18059–18074.

Coates, G. (2002). *The Rise and Fall of the Southern Alps*. Canterbury University Press, Christchurch, NZ.

Cotton, C. (1956). Coastal history of southern westland and northern fiordland. *Trans. R. Soc. NZ.*, 83:483–488.

Davey, F., Henyey, T., Holbrook, W., Okaya, D., Stern, T., Melhuish, A., Henrys, S., Anderson, H., Eberhart-Phillips, D., McEvilly, T., Uhrhammer, R., Wu, F., Jiracek, G., Wannamaker, P., Caldwell, G., and Christensen, N. (1998). Preliminary results from a geophysical study across a modern continent-continent collisional plate boundary - the southern alps, new zealand. *Tectonoph.*, 288:221–235.

Davey, F., Henyey, T., Kleffmann, S., Melhuish, A., Okaya, D., Stern, T., and Woodward, D. (1995). Crustal reflections from the alpine fault zone, south island, new zealand. *NZ. J. Geol. Geophys.*, 38:601–604.

Davey, F. and Smith, E. G. (1983). The tectonic setting of the fiordland region. *NZ. J. Geophys. J. R. Astron. Soc.*, 72:23–38.

Eberhart-Phillips, D. (1995). Examination in central alpine fault region, south island, new zealand. *NZ. J. Geol. Geophys.*, 38:571–578.

Garrick, R. and Hatherton, T. (1973). Seismic velocity studies in the southern alps, new zealand. *NZ. J. Geol. Geophys.*, 16(4):973–995.

Harrison, A. (1999). *Multi-channel seismic and flexural analysis of Westland Sedimentary Basin, South Island, New Zealand*. PhD thesis, Victoria University.

Hatherton, T. and Leopard, A. (1964). The densities of rocks. *NZ. J. Geol. Geophys.*, 7:605–625.

Herman, F. and Braun, J. (2007). Evolution of the glacial landscape of the southern alps of new zealand: insights from an ice erosion model. *J. Geophys. Res. (in press)*.

Holbrook, W., Okaya, D., Henyey, T., and Stern, T. (1996). Deep structure beneath the southern alps, new zealand from onshore-offshore wide-angle seismic data. *Trans. AGU*, 77(46):739.

Jongens, R. (2006). Gneissic rocks of the bonar range, central westland, new zealand. *NZ. J. Geol. Geophys.*, 49:281–286.

Kamp, P. J. and Tippett, J. (1993). Dynamics of pacific plate crust in the south island (new zealand) zone of oblique continent-continent convergence. *J. Geophys. Res.*, 98(B9):16105–16118.

Kleffmann, S. (1999). *Crustal structure studies of a transpressional plate boundary - the central South Island of New Zealand*. PhD thesis, Victoria University.

Kleffmann, S., Davey, F., Melhuish, A., Okaya, D., and Stern, T. (1998). Crustal structure in the central south island, new zealand, from the lake pukaki seismic experiment. *NZ. J. Geol. Geophys.*, 41:39–49.

Langdale, S. and Stern, T. (1998). Late tertiary deformation in cannington basin, south canterbury, new zealand: Evidence from seismic and gravity data. *NZ. J. Geol. Geophys.*, 41:247–257.

Leitner, B., Eberhart-Phillips, D., Anderson, H., and Nabelek, J. (2001). A focused look at the alpine fault new zealand: Seismicity, focal mechanisms, and stress observations. *J. Geophys. Res.*, 106(B2):2193–2220.

Little, T., Cox, S., Vry, J., and Batt, G. (2005). Variations in exhumation level and uplift rate along the oblique-slip alpine fault, central southern alps, new zealand. *GSA Bull.*, 117(5/6):707–723.

Little, T., Holcombe, R., and Ilg, B. (2002). Ductile fabrics in the zone of active oblique convergence near the alpine fault, new zealand: identifying the neotectonic overprint. *J. Stru. Geol.*, 24:193–217.

Mooney, W. and Ginzburg, A. (1986). Seismic measurements of internal properties of fault zones. *P. and Appl. Geophys.*, 124(1/2):141–158.

Nathan, S. (1977). Cretaceous and lower tertiary stratigraphy of the coastal strip between buttress point and ship creek, south westland, new zealand. *NZ. J. Geol. Geophys.*, 20(4):615–654.

Norris, R. and Cooper, A. (1995). Origin of small-scale segmentation and transpressional thrusting along the alpine fault, new zealand. *Geol. Soc. Am. Bull.*, 107(2):231–240.

Okaya, D., Christensen, N., Stanley, D., and Stern, T. (1995). Crustal anisotropy in the vicinity of the alpine fault zone, south island, new zealand. *NZ. J. Geol. Geophys.*, 38:579–583.

Okaya, D., Henrys, S., and Stern, T. (2002). Double-sided onshore-offshore seismic imaging of a plate boundary: "super-gathers" across south island, new zealand. *Tectonoph.*, 355:247–263.

Petit, J., Jouzel, J., Raynaud, D., Barkov, N., Barnola, J., Basile, I., Bender, M., Chappellaz, J., Davis, M., Delaygue, G., Delmotte, M., Kotlaykov, V., Legrand, M., Lipenkov, V., Lorius, C., Pepin, L., Ritz, C., Saltzman, E., and Stievenard, M. (1999). Climate and atmospheric history of the past 420,000 years from the vostok ice core, antarctica. *Nature*, 399:429–436.

Rattenbury, M. (1986). Late low-angle thrusting and the alpine fault, central westland, new zealand. *NZ. J. Geol. Geophys.*, 29(437-446).

Roberston, E. and Reilly, W. (1958). Bouguer anomaly map of new zealand. *NZ. J. Geol. Geophys.*, 1:560–564.

Scherwath, M., Okaya, D., Stern, T., Henrys, S., Kleffmann, S., and Davey, F. (1996). Sight'96 seismic land data acquisition report. *unpublished*.

Scherwath, M., Stern, T., Davey, F., Okaya, D., Holbrook, W., Davies, R., and Kleffmann, S. (2003). Lithospheric structure across oblique continental collision in new zealand from wide-angle p-wave modeling. *J. Geophys. Res.*, 108(B12):2566.

Sibson, R. (1977). Fault rocks and fault mechanisms. *J. Geol. Soc. London*, 133:191–213.

Sircombe, K. and Kamp, P. J. (1998). The south westland basin: seismic stratigraphy basin geometry and evolution of a foreland basin with the southern alps collision zone, new zealand. *Tectonoph.*, 300:359–387.

Sjögren, B. (1984). *Shallow refraction seismics*. Chapman and Hall.

Smith, E. G., Stern, T., and O'Brien, B. (1995). A seismic velocity profile across the central south island, new zealand. *NZ. J. Geol. Geophys.*, 38:565–570.

Stein, S. and Wysession, M. (2003). *An introduction to Seismology, Earthquake and Earth structure*. Blackwell Publishing.

Stern, T. (1995). Gravity anomalies and crust loading at and adjacent to the alpine fault, new zealand. *NZ. J. Geol. Geophys.*, 38:593–600.

Stern, T., Kleffmann, S., Okaya, D., Scherwath, M., and Bannister, S. (2001). Low seismic wave speeds and enhanced fluid pressure beneath the southern alps of new zealand. *Geology*, 29(8):679–682.

Stern, T. and McBride, J. (1998). Seismic exploration of continental strike-slip zones. *Tectonoph.*, 286:63–78.

Stern, T., Molnar, P., Okaya, D., and Eberhart-Phillips, D. (2000). Teleseismic p-wave and modes of shortening the mantle lithosphere beneath south island, new zealand. *J. Geophys. Res.*, 105(B9):21615–21631.

Suggate, R. (1963). The alpine fault. *Trans. R. Soc. NZ. (Geol.)*, 2(7):105–129.

Suggate, R. (1990). Late pliocene and quaternary glaciations of new zealand. *Quat. Sc. Rev.*, 9:175–197.

Suggate, R. and Almond, P. (2005). The last glacial maximum (lgm) in western south island, new zealand: implications for the global lgm and mis 2. *Quat. Sc. Rev.*, 24(16-17):1923–1940.

Sutherland, R. (1999). Cenozoic bending of new zealand basement terranes and alpine fault displacement: a brief review. *NZ. J. Geol. Geophys.*, 42:295.

Sutherland, R., Berryman, K., and Norris, R. (2006). Quaternary slip rates and geomorphology of the alpine fault: implications for kinematics and seismic hazard in southwest new zealand. *GSA Bull.*, 118(3/4):464–474.

Sutherland, R. and Norris, R. (1995). Late quaternary displacement rate, paleoseismicity, and geomorphic evolution of the alpine fault: evidence from hokuri creek, south westland, new zealand. *NZ. J. Geol Geophys*, 38:419–430.

Taylor, J. (1982). *An Introduction to error analysis - the study of the uncertainties in physical measurements*. University Science Book, Mill Valley, California.

Tippett, J. and Kamp, P. J. (1993). Fission track analysis of the late cenozoic vertical kinematics of continental pacific crust, south island, new zealand. *J. Geophys. Res.*, 98(B9):16119–16148.

Toulmin, S. J. (2006). *Galatea Basin: the geophysical exploration of a transtensional basin in the southern Bay of Plenty, New Zealand*. Masters thesis, Victoria University of Wellington, Wellington.

Walcott, R. (1979). Plate motion and shear strain rates in the vicinity of the southern alps. *Bull. R. Soc. NZ.*, 18:5–12.

Walcott, R. (1998). Modes of oblique compression: Late cenozoic tectonics of the south island of new zealand. *Rev. Geophys.*, 36(1):1–26.

Wellman, H. (1979). An uplift map for the south island of new zealand, and a model for the uplift of the southern alps. *Bull. R. Soc. NZ.*, 18:13–20.

Wightman, R. and Little, T. (2007). *Deformation of the pacific plate above the alpine fault ramp and its relationship to expulsion of metamorphic fluids: an array of backshears*, volume 175 of *Tectonics of a continental transform plate boundary: the south island, new zealand: AGU monograph Series*.

Woodward, D. (1979). The crustal structure of the southern alps, new zealand, as determined by gravity. *Bull. R. Soc. NZ.*, 18:95–98.

Young, D. (1968). The fraser fault in central westland, new zealand, and its associated rocks. *NZ. J. Geol. Geophys.*, 11(2):291–311.

Zelt, C. (1999). Modeling strategies and model assessment for wide-angle seismic traveltime data. *Geophys. J. Int.*, 139:183–204.